Journal of Magnetism and Magnetic Materials 659 (2026) 174669



Contents lists available at ScienceDirect

Journal of Magnetism and Magnetic Materials

journal homepage: www.elsevier.com/locate/jmmm



Research article

Self-organization of magnetic nanoparticles in a viscous fluid via dipolar interactions☆

Ludovic Godard-Cadillac [a], Paul-Antoine Hervieux [b], Giovanni Manfredi [b,*]

[a] Université de Bordeaux, Bordeaux INP, Institut de Mathématiques de Bordeaux, UMR 5251, F-33400 Talence, France
[b] Université de Strasbourg, CNRS, Institut de Physique et Chimie des Matériaux de Strasbourg, UMR 7504, F-67000 Strasbourg, France

ARTICLE INFO

Keywords:
Magnetic nanoparticles
Modeling and simulations
Dipolar interactions
Thermal effects
Solvent

ABSTRACT

We investigate numerically the dynamics of monodomain magnetic nanoparticles (NPs) suspended in a viscous fluid, interacting through dipolar magnetic forces with moments constrained along their easy axes. The model includes particle inertia, viscous drag, and short-range repulsion to prevent overlap. For small systems, the NPs self-assemble into linear and ring-like aggregates; increasing the particle number induces a transition toward filamentous structures featuring junctions ('triple points') where one NP connects to three neighbors. A statistical analysis quantifies the decline of simple aggregates and the rise of filamentous networks with system size. We then examine the thermal stability of these structures, both in an ideal fluid and in 1-octadecene. The simulations reveal temperature-dependent rearrangements driven by the competition between thermal agitation and magnetic bonding, with clear correlations between changes in potential energy and the onset of configurational transformations.

1. Introduction

The precise assembly of nanoscale objects into organized superstructures remains a central challenge in nanoscience, with far-reaching implications for the rational design of functional materials, biomedical platforms, and nanoengineered devices.

Magnetic nanoparticles (NPs) represent a particularly versatile class of nanomaterials, distinguished by their superparamagnetic properties, tunable surface chemistry, and responsiveness to externally applied magnetic fields. Owing to these attributes, magnetic NPs have found widespread applications, including water remediation [1], as well as diagnostic and therapeutic uses in ferrofluid-based biomedical technologies [2–4]. Recent reviews have highlighted their expanding role for various applications [5,6].

At the core of magnetic NP self-organization lies the magnetic dipole–dipole interaction, arising from the intrinsic magnetic moments of the particles. This interaction modulates interparticle forces, dictates assembly dynamics, and governs the structural patterns that emerge in NP assemblies. These magnetic features lend themselves to a variety of technological applications, including data storage [7,8], sensing [9,10], spintronics and electronic transport [11–13], magnetic imaging [14], and magnetic hyperthermia [15,16].

Ferrofluids – colloidal suspensions of ferromagnetic particles in carrier liquids – exemplify the tunability of dipolar interactions in magnetic systems [17,18]. When external magnetic fields are applied, ferrofluids exhibit a remarkable ability to self-organize and support dynamic morphologies. This has enabled advanced material synthesis strategies [19], as well as the realization of complex magnetically driven behaviors such as collective oscillations and pattern formation [20–23]. Magnetic dipolar interactions play a key role in these applications, facilitating structural assembly and inducing the coupling between the magnetization dynamics and the particle motion, both vibrational and translational.

Previous studies have investigated the stability of magnetic NP clusters using global energy minimization approaches, which reveal preferred superstructures dependent on particle number [24–26]. Langevin dynamics simulations have also been employed to study the behavior of NP systems, both with and without applied magnetic fields, including polymer-linked colloidal particles [27–29]. Additional investigations have explored magnetic NP distributions in ferrofluids [30], aggregation dynamics during fluid evaporation [31], clustering behavior on magnetized substrates [32], and clustering phenomena in colloidal NP systems [33].

Considerable effort has also been devoted to understanding the equilibrium self-assembly of dipolar magnetic NPs. Using Monte Carlo simulations, Kantorovich et al. [34] demonstrated how thermal fluctuations induce structural transitions between chains, rings, and more

☆ This article is part of a Special issue entitled: 'Magnetic Nanoparticles (ICFPM 2025)' published in Journal of Magnetism and Magnetic Materials.

* Corresponding author.
E-mail address: giovanni.manfredi@ipcms.unistra.fr (G. Manfredi).

https://doi.org/10.1016/j.jmmm.2026.174669
Received 19 February 2026; Received in revised form 5 October 2026; Accepted 7 October 2026
Available online 13 October 2026
0304-8853/© 2026 The Authors. Published by Elsevier B.V. This is an open access article under the CC BY license (http://creativecommons.org/licenses/by/4.0/).

compact aggregates through the competition between dipolar interactions and entropy. More recently, Solovyova et al. [35], also using Monte Carlo simulations, studied the formation of nanoparticle aggregates in confined volumes and analyzed the relationship between the morphology of the aggregates and their magnetic response. These studies have considerably improved our understanding of equilibrium structures in dipolar colloids. The present work adopts a complementary perspective by focusing on the nonequilibrium dynamical pathways leading to these structures. Our objective is not only to characterize the final aggregates, but also to understand the mechanisms governing their formation, their statistical properties, their stability against thermal fluctuations, and their response to external magnetic fields.

Here, we build upon a simplified yet physically grounded model describing the dynamics of identical spherical magnetic NPs suspended in a viscous fluid [36]. Each particle is characterized by its translational and rotational velocities, magnetic moment, and spatial position, evolving under the influence of dipole–dipole magnetic forces, viscous drag, and short-range repulsive contact interactions that prevent overlap. The magnetic interaction is modeled via the classical dipolar potential, while the fluid medium is treated as a static background, consistent with the low Reynolds number typical at nanoscales. The earlier unpublished work [36] contained preliminary results on the stability of NP structures and their linear response to external perturbations. Here, we provide an exhaustive treatment of the NP dynamics and thermodynamics, as well as a systematic statistical investigation of the various NP configurations.

The primary objective of this study is to investigate the mechanisms by which NP assemblies evolve toward equilibrium configurations under varied physical constraints. Through molecular dynamics simulations, we investigate the spontaneous emergence of structures such as linear chains (“spears”), circular rings, and filamentous networks featuring multi-branched junctions referred to as “triple points”. These configurations arise as the system dissipates energy and settles into local minima of the interaction potential. Furthermore, we analyze how structural stability depends on the number of particles and the fluid temperature. We identify a wide range of phenomena with very different time scales, ranging from $\approx 0.1\,\mu s$ for binary particle–particle interactions to $\approx 1\,ms$ for thermal relaxation. These diverse time scales span four order of magnitudes, making their numerical simulation a particularly complex task.

Such linear and circular structures have been studied from a mathematical viewpoint in [37], using techniques from the calculus of variations. In that work, the authors establish existence and uniqueness results, derive bounds on the distance between neighboring particles, and provide an asymptotic description as the number of particles tends to infinity. Specifically, they show that the typical distance between the centers of the NPs converges toward an explicit limit. Here, in contrast, we focus on the dynamical and thermodynamical properties of these structures—e.g., how they self-assemble, how they respond to external magnetic fields, and how their properties are modified by thermal effects; we also provide statistical estimates of their probability to emerge from random initial conditions.

A noteworthy contribution of our study is the concept of *magnetic bonds* – stable pairwise alignments of magnetic dipoles – which provides a physically intuitive and quantitatively useful framework for understanding structural evolution and stability. We further examine the role of externally applied magnetic fields and geometric confinement in two dimensions, conditions that are experimentally relevant in microscopy techniques such as transmission electron microscopy and magnetic force microscopy [38]. The findings presented here provide new insight into the self-organization of dipolar colloidal systems and offer a foundation for controlled NP assembly in future applications.

Finally, thermal effects are modeled by incorporating a stochastic noise term in the governing equations, enabling us to describe thermally activated rearrangements in the system. The numerical results reveal how thermal effects can disrupt the magnetic structures – both rings and spears – through multiple structural transitions, ultimately leading to a system constituted of isolated NPs.

The remainder of this paper is organized as follows. Section 2 introduces our mathematical model of magnetic NPs immersed in a viscous fluid, incorporating both mechanical motion and magnetic dynamics. Section 3 provides an exhaustive statistical analysis of the properties of the NP ensemble in the absence of thermal fluctuations, including the effect of an external magnetic field and the geometry of the system (three- or two-dimensional). In Section 4, we study the influence of thermal fluctuations for an idealized solvent endowed with temperature-independent viscosity. Section 5 extends the analysis of thermal effects to the case of a realistic solvent, namely 1-octadecene, which is commonly employed in the synthesis of magnetic NPs. Conclusions are summarized in Section 6.

2. Dynamical model of magnetic NP assemblies

The present model of magnetic NPs immersed in a viscous fluid was first developed in [36]. Although simple, this model can yield very rich and complex solutions, both static and dynamic. Each magnetic NP is represented as an element of $\mathbb{R}^3 \times \mathbb{R}^3 \times \mathbb{S}^2$, where $\mathbb{S}^2$ is the sphere of unit radius. The first three coordinates ($\boldsymbol{x} \in \mathbb{R}^3$) represent the position of the center of the NP, while the second three ($\boldsymbol{\omega} \in \mathbb{R}^3$) represent their angular velocity. Finally, $\boldsymbol{m} = (\sin\theta\cos\phi,\ \sin\theta\sin\phi,\ \cos\theta) \in \mathbb{S}^2$ represents the direction of the magnetic moment of the NP, parameterized using the spherical angles ϕ and θ.

We consider a system of N identical spherical NPs, described by the variables $(\boldsymbol{x}_i, \boldsymbol{\omega}_i, \boldsymbol{m}_i)$, with $i = 1, \dots N$, immersed in a fluid characterized by dynamic viscosity η. At the nanometric scale, the Reynolds number is so small that one can assume the fluid to be immobile with respect to the motion of the NPs. In other words, there is no backreaction of the NPs on the viscous fluid, which only acts as a source of friction (negative drag) on the NPs. We define the friction coefficients for translations and rotations as:

$$\zeta_t = 6\pi\eta R, \qquad \text{and} \qquad \zeta_r = 8\pi\eta R^3,$$

where R is the radius of the NP. Newton's second law reads as:

$$M\frac{d^2}{dt^2}\boldsymbol{x}_i = \boldsymbol{F}_i - \zeta_t\frac{d}{dt}\boldsymbol{x}_i, \quad i = 1, \dots, N \tag{1}$$

where M represents the mass of the NP and $\boldsymbol{F}_i$ is the sum of all the conservative forces applied to the i-th NP. As to the rotation dynamics, we write:

$$I\frac{d}{dt}\boldsymbol{\omega}_i = \boldsymbol{T}_i - \zeta_r\boldsymbol{\omega}_i, \quad i = 1, \dots, N, \tag{2}$$

where $\boldsymbol{T}_i$ is the conservative part of the torque and $I = 2MR^2/5$ is the principal moment of inertia of a homogeneous spherical particle.

We recall the expression of a magnetic field generated by a magnetic dipole $\boldsymbol{m}$ centered at the origin of the axes $(0,0,0)$:

$$\boldsymbol{B}^d = \frac{\mu_0\mu_s^2}{4\pi}\frac{3(\boldsymbol{m}\cdot\boldsymbol{e}_r)\boldsymbol{e}_r - \boldsymbol{m}}{|\boldsymbol{x}|^3},$$

where $\boldsymbol{e}_r = \boldsymbol{x}/|\boldsymbol{x}|$ is the unit radial vector and μ_s is the magnetization at saturation (magnetic moment of a single atom times the number of atoms in the NP). Here, we will consider cobalt NPs, for which the magnetic moment of a single atom is equal to $1.7\mu_B$, where μ_B denotes the Bohr magneton.

We denote by $\boldsymbol{B}_i$ the total magnetic field observed at point $\boldsymbol{x}_i$, which is the sum of the dipolar fields generated by all the other NPs. It is then possible to write the magnetic torque induced by $\boldsymbol{B}_i$ on the ith NP:

$$\boldsymbol{T}_i = \boldsymbol{m}_i \times \boldsymbol{B}_i. \tag{3}$$

In order to write the conservative part of the force in Eq. (1), we first introduce the magnetic interaction potential:

$$U_{ij}^d = -\boldsymbol{m}_j \cdot \boldsymbol{B}_i = \frac{\mu_0\,\mu_s^2}{4\pi}\left[\frac{\boldsymbol{m}_i\cdot\boldsymbol{m}_j}{|\boldsymbol{r}_{ij}|^3} - 3\frac{(\boldsymbol{m}_i\cdot\boldsymbol{r}_{ij})(\boldsymbol{m}_j\cdot\boldsymbol{r}_{ij})}{|\boldsymbol{r}_{ij}|^5}\right],$$

where $\boldsymbol{r}_{ij} = \boldsymbol{x}_i - \boldsymbol{x}_j$. We can compute the forces exerted by dipole j on dipole i, which gives by direct computation:

$$\boldsymbol{F}_{ij}^d = -\nabla U_{ij}^d = \frac{\mu_0 \mu_s^2}{4\pi} \frac{3}{|\boldsymbol{r}_{ij}|^5} \left[(\boldsymbol{m}_i \cdot \boldsymbol{r}_{ij})\boldsymbol{m}_j + (\boldsymbol{m}_j \cdot \boldsymbol{r}_{ij})\boldsymbol{m}_i + (\boldsymbol{m}_i \cdot \boldsymbol{m}_j)\boldsymbol{r}_{ij} - 5\frac{(\boldsymbol{m}_i \cdot \boldsymbol{r}_{ij})(\boldsymbol{m}_j \cdot \boldsymbol{r}_{ij})}{|\boldsymbol{r}_{ij}|^2}\boldsymbol{r}_{ij} \right]. \tag{4}$$

We then have the dipolar part of the conservative force:

$$\boldsymbol{F}_i^d = \sum_{\substack{j=1 \\ j\neq i}}^{N} \boldsymbol{F}_{ij}^d.$$

Finally, the collisions between the NPs are modeled by a repulsive potential with the form:

$$U_{ij}^s = 2C_s \left(\frac{2R}{|\boldsymbol{r}_{ij}|} \right)^{\alpha},$$

where $\alpha > 3$, so that the repulsive term is dominant for small interparticle distances (when the distance is smaller than $2R$). We then choose the constant C_s to properly represent the fact that R is the radius of the NP. More precisely, the two energies (magnetic and repulsive) must be balanced when two NPs have their mutual centers at distance $2R$, with their magnetic moments aligned in the same direction. This leads to the following definition:

$$C_s = \frac{\mu_0 \mu_s^2}{4\pi R^3}.$$

The associated repulsive force is:

$$\boldsymbol{F}_{ij}^s = -\nabla U_{ij}^s = \frac{\alpha C_s}{2R} \left(\frac{2R}{|\boldsymbol{r}_{ij}|} \right)^{\alpha+1} \frac{\boldsymbol{r}_{ij}}{|\boldsymbol{r}_{ij}|}. \tag{5}$$

We then set $\boldsymbol{F}_i^s = \sum_{j\neq i} \boldsymbol{F}_{ij}^s$ the total repulsive force, and $\boldsymbol{F}_i = \boldsymbol{F}_i^d + \boldsymbol{F}_i^s$ the total force acting on the ith particle.

To close the system, we need to make the connection between the mechanical motion of the NP and the dynamics of its magnetic moment $\boldsymbol{m}_i$, leading to an equation for $d\boldsymbol{m}_i/dt$. To start with, we write:

$$\left.\frac{d\boldsymbol{m}_i}{dt}\right|_{\mathcal{R}} = \left.\frac{d\boldsymbol{m}_i}{dt}\right|_{\mathcal{R}'} + \boldsymbol{\omega}_i \times \boldsymbol{m}_i, \tag{6}$$

where $\mathcal{R}$ is the reference frame of the laboratory and $\mathcal{R}'$ is the frame attached to a NP that rotates with angular velocity $\boldsymbol{\omega}_i$ in the frame $\mathcal{R}$.

The evolution of the magnetization in the frame $\mathcal{R}'$ of the NP is given by the Landau–Lifschitz–Gilbert (LLG) equation [39]. Here, the NPs are supposed to be monodomain (because of their small size) with uniaxial anisotropy along the "easy" magnetization axis. We also suppose the anisotropy energy is sufficiently large for the NP not to enter the superparamagnetic regime, where its magnetization would randomly switch between two opposite directions due to thermal fluctuations. Given these hypotheses, the damping term in the LLG equation tends to drive the magnetic moment toward the easy magnetization axis. This alignment occurs on a scale much faster than the typical timescale of the NP dynamics [40]. It is therefore assumed here that the magnetic moment is immobile in the frame associated with the NP, and Eq. (6) reduces to:

$$\frac{d}{dt}\boldsymbol{m}_i = \boldsymbol{\omega}_i \times \boldsymbol{m}_i. \tag{7}$$

The main purpose of this work is to study numerically the system of Eqs. (1), (2), (3), (4), (5), (7), which governs the dynamics of magnetic NPs in a viscous fluid. In the absence of the viscous term (that is, if $\eta = 0$), this system preserves the total energy (sum of the kinetic and potential energies), where the total potential energy U is defined as:

$$U = U^d + U^s = \sum_{i\neq j} U_{ij}^d + \sum_{i\neq j} U_{ij}^s.$$

The kinetic energy

$$K = K^t + K^r = \sum_{i=1}^{N} \frac{M}{2} \left(\frac{d\boldsymbol{x}_i}{dt} \right)^2 + \sum_{i=1}^{N} \frac{I}{2} \boldsymbol{\omega}_i^2$$

is the sum of its translational and rotational components. In addition, if the sum of the external forces acting on the NPs is equal to zero, the total linear momentum $\boldsymbol{P} = \sum_i \boldsymbol{p}_i = \sum_i M\, d\boldsymbol{x}_i/dt$ is also conserved.

Each NP also possesses an intrinsic angular momentum: $\boldsymbol{S}_i = I\boldsymbol{\omega}_i$, which arises from its rotational motion around its center of mass. Additionally, it has an "orbital" angular momentum, given by $\boldsymbol{L}_i = \boldsymbol{x}_i^* \times \boldsymbol{p}_i^*$, which is due to the movement of the NP around the center of mass of the entire system, i.e., $\boldsymbol{x}_i^* = \boldsymbol{x}_i - \boldsymbol{x}_{\mathrm{cm}}$ and $\boldsymbol{p}_i^* = \boldsymbol{p}_i - \boldsymbol{p}_{\mathrm{cm}}$. The total angular momentum of the system is then given by

$$\boldsymbol{J} = \sum_{i=1}^{N} (\boldsymbol{L}_i + \boldsymbol{S}_i).$$

In the absence of viscosity, each component of this total angular momentum is conserved.

In the present work, we consider systems with viscosity high enough to display a strong dissipation of the energy by interaction with the fluid. In that case, the system converges toward a local minimum of the energy in which the NPs create structures with very diverse geometric properties.

3. Numerical results without thermal fluctuations

In this section, we present the results of simulations conducted in the absence of thermal fluctuations. The results are obtained by numerical resolution of the equations of motion detailed in the preceding section. Since our model consists of a set of ordinary differential equations, its numerical integration does not require specifying a computational box. Further details on the numerical techniques are provided in Appendix A.

We analyze the structures that spontaneously emerge as the system evolves toward equilibrium – corresponding to a local minimum of the interaction potential – where all the kinetic energy is dissipated through viscous coupling with the surrounding fluid.

The formation of these structures is driven by the characteristics of the magnetic dipole–dipole interaction: NPs experience attractive forces that are proportional to the relative alignment of their magnetic moments and inversely proportional to the fourth power of their mutual separation distance. This anisotropic and long-range interaction promotes the self-organization of the particles into energetically favorable configurations.

We consider a system of identical cobalt NPs with the following characteristics: radius $R = 5\,\mathrm{nm}$; mass $M = 9 \times 10^{-22}\,\mathrm{kg}$; magnetic moment at saturation $\mu_s = 2{\times}10^{-19}\,\mathrm{A\,m^2}$. For the solvent, we employ an idealized fluid with temperature-independent dynamic viscosity close to that of water at 330 K, i.e., $\eta = 0.5\,\mathrm{mPa\,s}$. Although idealized, this configuration enables us to perform an in-depth study of the NPs/solvent system, including the effect of thermal fluctuations (see Section 4).

3.1. Qualitative analysis of the observed structures

3.1.1. Simple structures for small N

We first present the numerical results obtained with a small number of particles N. Two types of geometries emerge clearly from these simulations (see Figs. 1, 2, and 3), which we term "rings" and "spears":

- **Ring**: this structure corresponds to the situation where the NPs are equi-distributed on a circle and their magnetic moments are pointing in the direction parallel to the circle. This configuration is unstable for $N = 2$ (Fig. 1) and becomes stable when $N \geq 3$ (Fig. 2).
- **Spear**: this structure corresponds to the situation where all the NPs are aligned and their magnetic moments also point in the same direction. When $N = 2$, it is straightforward to prove that this is the only stable stationary point and that it is a global attractor for the dynamics. The spear structure is stable for all N (Fig. 3) [37].

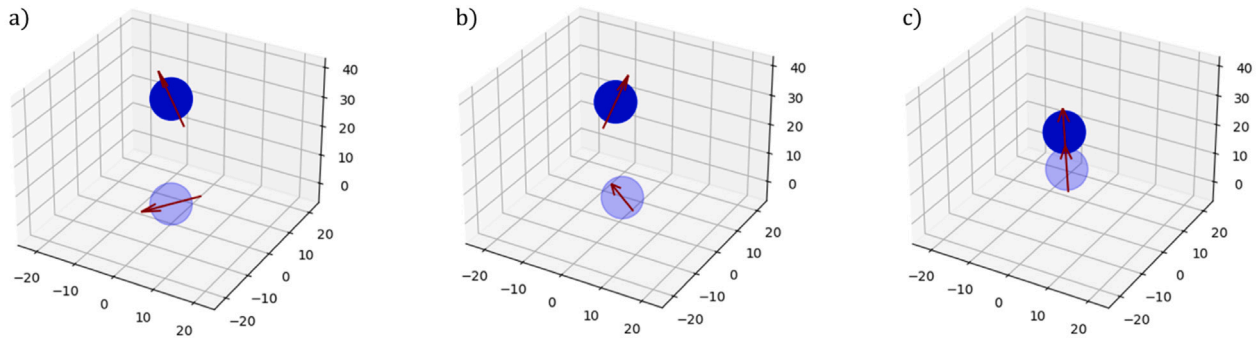


Fig. 1. Dynamics of $N = 2$ particles in 3D space at three different times during the evolution: $t = 0$ ns (a), $t = 50$ ns (b), and $t = 100$ ns (c).

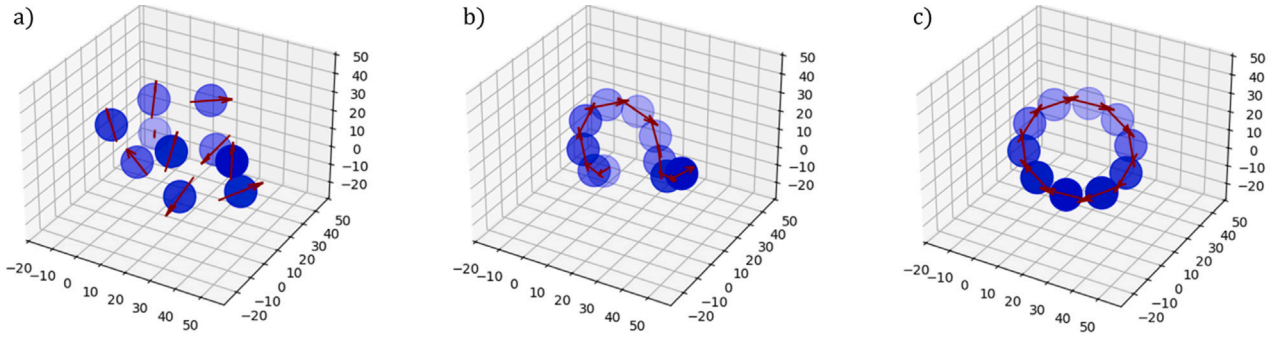


Fig. 2. Dynamics of $N = 10$ NPs in 3D space at three different times during the evolution: $t = 0$ ns (a), $t = 100$ ns (b), and $t = 200$ ns (c). The emergence of a ring structure is clearly visible. Space coordinates are expressed in nm.

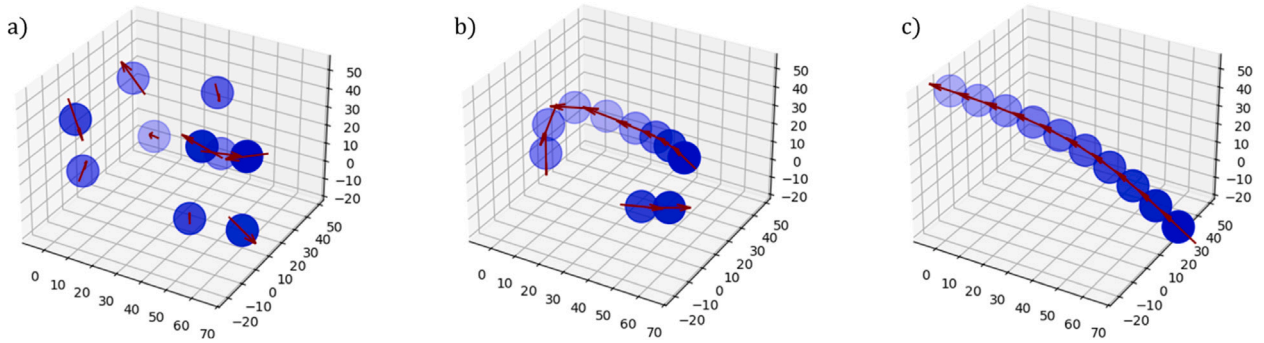


Fig. 3. Dynamics of $N = 10$ NPs at three different times during the evolution: $t = 0$ ns (a), $t = 100$ ns (b), and $t = 200$ ns (c). At $t = 200$ ns, a spear structure has emerged. Space coordinates are expressed in nm.

The NPs are initially distributed randomly in the computational box, with random orientations of their magnetic moments. Hence, the emergence of either a spear or a ring structure depends uniquely (at least for $N > 2$) on the initialization of the system.

3.1.2. Complex structures for large N

The NPs are initially distributed randomly in the computational box, and separated on average by a distance of a few ($\approx 3-6$) particle radii R. Hence, the NP concentration is approximately the same, irrespective of the number of NPs. For instance, in the forthcoming simulation with $N = 343$, we computed an average distance of $5.4R$. The corresponding volume fraction occupied by the particles is 21 %. The NP concentration is therefore not an independent control parameter in the present N-dependence study. A systematic investigation of concentration effects on the formation of large-N structures is beyond the scope of the present work. Experimentally, concentration and the number of particles participating in a given aggregate should be regarded as related but distinct control parameters.

As the number of particles increases, the NPs continue to exhibit local magnetic alignment and attraction; however, more complex structural behaviors begin to emerge. One of the first notable phenomena is the appearance of multiple disconnected simple structures, such as spears and rings, which interact magnetically without coalescing into a single aggregate [Fig. 4(a), (b), (c)]. In addition, we observe the formation of filamentous assemblies interconnected via specific junctions, termed *triple points*, where a single NP connects to three neighbors instead of the usual two [Fig. 4(d), (e), (f)]. When the number of particles becomes significantly large (several hundreds), the system evolves, over long timescales, into a highly complex configuration composed of elongated filamentous structures. These filaments are frequently intertwined and interconnected through triple points, where individual NPs simultaneously bind to three neighbors (Fig. 5). In many instances, the resulting structure comprises several connected components of varying sizes. The smallest components often adopt ring-like configurations. These findings reveal the emergent organization driven by long-range dipolar interactions in large NP systems.

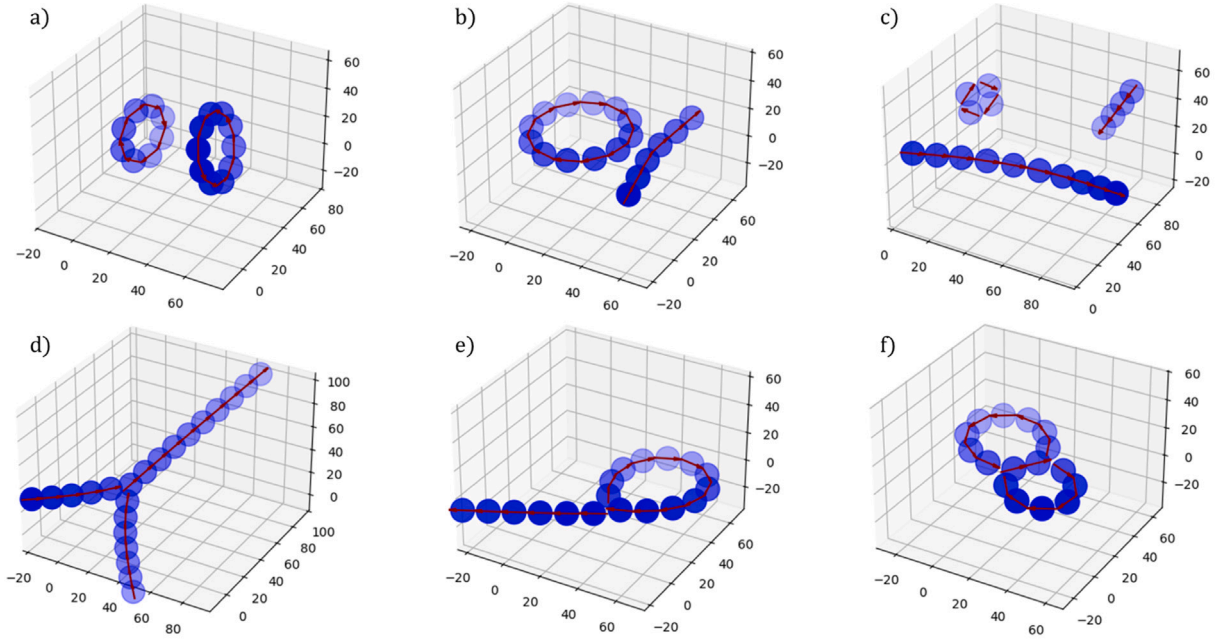


Fig. 4. Emergence of more complex structures as the number of particles increases. Panels (a), (b) and (c) show cases where disconnected structures emerge, either spears or rings, or both. Panels (d), (e) and (f) show cases displaying triple points with respectively 0, 1 and 2 loops. The number of NPs ranges from $N = 16$ to $N = 22$. Space coordinates are expressed in nm.

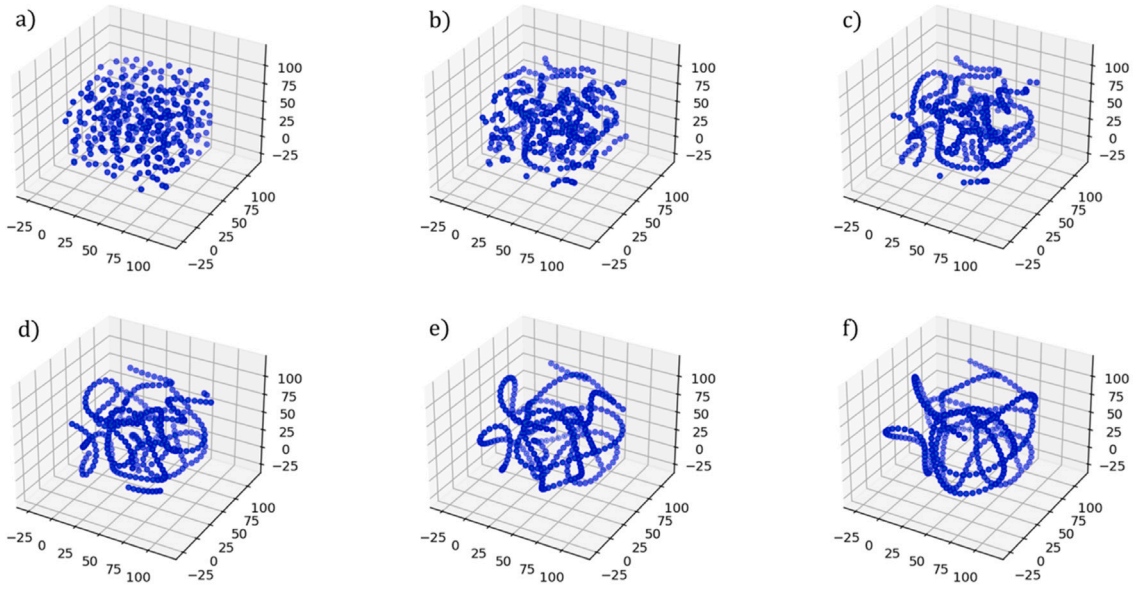


Fig. 5. Configurations of $N = 343$ NPs, at times $t = 0$, 1, 3, 10, 50, and 100 μs (from top left to bottom right panels). Space coordinates are expressed in nm.

3.2. Statistical analysis of the structures

In order to elucidate this phenomenon of disappearing of simple structure for more complex ones, we perform here some statistical analysis. We run the simulations 500 times with random initial conditions until convergence of the dynamics through viscous dissipation. We then compute several statistical indicators (defined and discussed in Appendix B) for the different structures appearing in the final configurations. These indicators provide a probability of presence for a given structure: spear, ring, or a structure that is neither aligned nor circular. We perform this analysis for different numbers of NPs (from $N = 2$ to $N = 25$) and thus quantify the emergence of complex structures as the number of NPs rises. The obtained results are plotted in Fig. 6.

Fig. 6(a) represents the number of stationary structures exhibiting at least one connected components that is a spear. This configuration dominates when the number of NPs is small. For $N = 2$, this is actually the only stable arrangement, as can be shown by direct computation [37]. As the number of particles increases, the spear structures tend to disappear. However, the histograms do not vanish entirely. Indeed, further investigations showed that when $N \geq 20$ the presence of a spear is correlated to the appearance of disconnected structures: the conditional probability of observing a disconnected structure given the presence of a spear reaches unity at $N = 25$. In summary, while spear configurations are strongly favored in small systems, they become extremely rare as particle number increases. Only specifically prepared initial conditions converge to these configurations

in the large-N regime, where they remain stable but exhibit a markedly reduced basin of attraction.

Fig. 6(b) displays the number of stationary configurations containing at least one connected component identified as a ring. The ring structure becomes increasingly prevalent as the number of NPs increases, reaching a maximum occurrence at $N = 14$, followed by a slight decline for larger values of N. As in the case of spear configurations, we observe a high conditional probability of encountering disconnected components when a ring is present. This trend suggests that rings predominantly emerge as small substructures that are magnetically isolated from the rest of the system, rather than forming a single large ring encompassing all 25 NPs. However, the conditional probability of observing a disconnected structure given the presence of a ring is only 0.65, indicating that rings made of 25 NPs are not rare. Unlike the spear configuration, rings remain relatively frequent and robust even for large particle counts. Interpreting this data in terms of structural stability, the prevalence of rings implies a higher likelihood of formation and persistence compared to spears. This enhanced stability will be confirmed in subsequent analyses that incorporate thermal effects.

Fig. 6(c) shows the number of stationary configurations containing at least one connected component that is neither a ring nor a spear. Direct visual inspection indicates that these structures – hereafter referred to as "complex structures" – typically feature at least one triple point, where a single NP is connected to three neighbors, as shown in Fig. 4(d)–(f). This histogram clearly demonstrates that the structural complexity of the assembly increases with the number of NPs.

Fig. 6(d) presents the number of long-time configurations that exhibit disconnected components. This quantity also increases with N, consistent with the growing likelihood of fragmentation and the coexistence of multiple substructures as the number of NPs rises.

Finally, for all simulations with particle numbers ranging from $N = 2$ to $N = 25$, configurations containing more than two connected components were extremely rare, occurring only 5 times out of more than 10^4 simulations. Therefore, the four histograms presented in Fig. 6 offer a comprehensive and representative characterization of the structural complexity as a function of N. Error bars were computed using the standard Wilson formula with 95 % margin.[1]

3.3. Effect of an external magnetic field and planar confinement

In this section, we present additional simulation results without thermal fluctuations, aimed at investigating two distinct physical scenarios: (i) the influence of an externally applied magnetic field and (ii) the structural evolution of the system when the NP dynamics is constrained to a 2D plane.

External magnetic field. An external uniform magnetic field is incorporated by modifying the magnetic field B_i appearing in the equations of motion by adding a constant uniform field. Without loss of generality, we consider a field oriented along the z-axis: $\boldsymbol{B}_{\text{ext}} = B_{\text{ext}}\,\boldsymbol{e}_z$. As a representative case, we use the final structure depicted in Fig. 5 at $t = 100\,\mu\text{s}$ as the initial condition, and apply an external field of magnitude $B_{\text{ext}} = 100\,\text{mT}$, which is easily available for experiments. Numerical estimates suggest that the magnetic field induced by neighboring particles lies approximately in the range 10–100 mT, depending on the local curvature of the structure. Accordingly, the imposed field is expected to disrupt most, if not all, of the magnetic bonds.

[1] These error bars should be considered with caution since it is unclear whether the standard statistical hypothesis (independence and identical distribution) is satisfied or not. In general, solving a differential equation numerically breaks down the independence and identical distribution satisfied at the initial time. Yet, it provides a useful indication on the reliability of the results.

Simulation results are presented in Fig. 7. As anticipated, the external field progressively disrupts magnetic bonding between NPs, leading to the disappearance of both ring-like structures and triple points. The magnetic moments increasingly align with the applied field, resulting in the reorganization of the system into spear-like assemblies oriented parallel to $\boldsymbol{B}_{\text{ext}}$. Over long timescales, these spear structures become uniformly aligned and remain motionless relative to one another.

Dynamics constrained on a plane. Complex three-dimensional structures formed by NP ensembles are challenging to observe experimentally, as electron transmission can be significantly attenuated by the thickness of the sample. To overcome this limitation, various experimental techniques have been developed to constrain the NPs within two-dimensional (2D) geometries [41].

To investigate this scenario numerically, we performed a series of simulations involving $N = 324$ magnetic NPs using the same equations of motion described previously. The primary modification consists in enforcing the constraint $z = 0$ throughout the simulation, thereby confining particle positions to a plane. It is important to note that their magnetic moments remain free to rotate on the unit sphere $\mathbb{S}^2$, thus preserving their 3D nature. This planar confinement is implemented numerically by projecting each particle's position onto the $z = 0$ plane at every time step.

The simulation is conducted in two stages, as illustrated in Fig. 8.

First, the system of NPs is initialized with a random configuration and allowed to evolve freely within the (x, y) plane. Over time, the system exhibits the spontaneous formation of filamentous structures interconnected by triple points, similarly to what was previously observed in a 3D setting, now projected onto a plane. These filaments appear to exhibit a characteristic length scale, likely governed by curvature-dependent stability. Detailed inspection of the dynamics reveals that magnetic bonds between neighboring particles form and break frequently, until the system settles into a stable energy basin.

At a second stage, an external magnetic field $B_{\text{ext}} = 100\,\text{mT}$ is applied within the (x, y) plane to investigate its influence on structural evolution. As expected, this field induces a progressive disruption of magnetic bonds, leading to the breakdown of triple points and the alignment of the NP structures with the external field. The long-time configuration with an external field resembles that observed in the 3D case: a collection of spear-like structures, aligned parallel to the field and spatially disconnected. These spears exhibit negligible relative motion, stabilizing as static arrangements parallel to the external magnetic field.

4. Thermal effects

This section investigates the influence of a finite solvent temperature on the emergence and stability of NP structures. Temperature effects are incorporated by adding Gaussian white noise into the translational and rotational evolution Eqs. (1) and (2) [36]. These stochastic terms take the form of a fluctuating force and torque, with zero average and no memory (Markovian process):

$$\langle F_{\text{st}}^{\alpha}(t)\rangle = 0, \quad \langle F_{\text{st}}^{\alpha}(t)\, F_{\text{st}}^{\beta}(t')\rangle = 2k_B T\, \zeta_{\text{t}}\, \delta_{\alpha\beta}\, \delta(t-t')$$

and

$$\langle T_{\text{st}}^{\alpha}(t)\rangle = 0, \quad \langle T_{\text{st}}^{\alpha}(t)\, T_{\text{st}}^{\beta}(t')\rangle = 2k_B T\, \zeta_{\text{r}}\, \delta_{\alpha\beta}\, \delta(t-t'), \tag{8}$$

where T is the temperature of the ambient fluid, k_B denotes Boltzmann's constant, $\delta(t)$ and $\delta_{\alpha\beta}$ are respectively the Dirac and Kronecker delta functions, the indices α, β correspond to the three Cartesian coordinates in $\mathbb{R}^3$, and $\langle \dots \rangle$ denotes ensemble average (average over different statistical realizations). Further details on the numerical scheme with thermal effects are given in Appendix A.2.

In this section, we shall consider an idealized situation where the dynamic viscosity of the solvent does not depend on the temperature and is close to that of water at 330 K ($\eta = 0.5\,\text{mPa s}$).

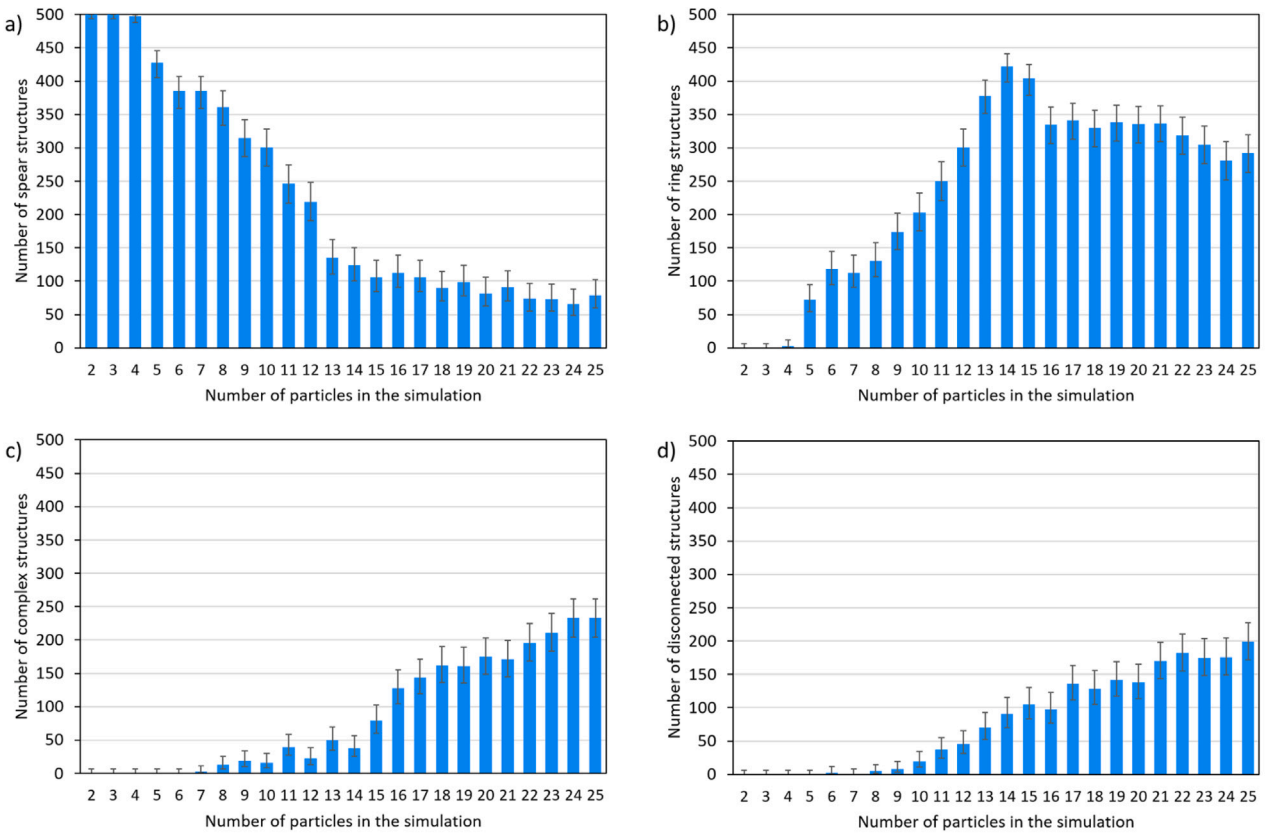


Fig. 6. Histograms quantifying the presence of various structures obtained with 500 different initial conditions, for systems comprising $N = 2, \ldots, 25$ NPs. We show the number of long-time stationary structures that have a connected component that is a spear (a), a ring (b), neither a spear nor a ring (c), or a disconnected structure (d). Error bars were computed using the standard Wilson formula with 95 % margin.

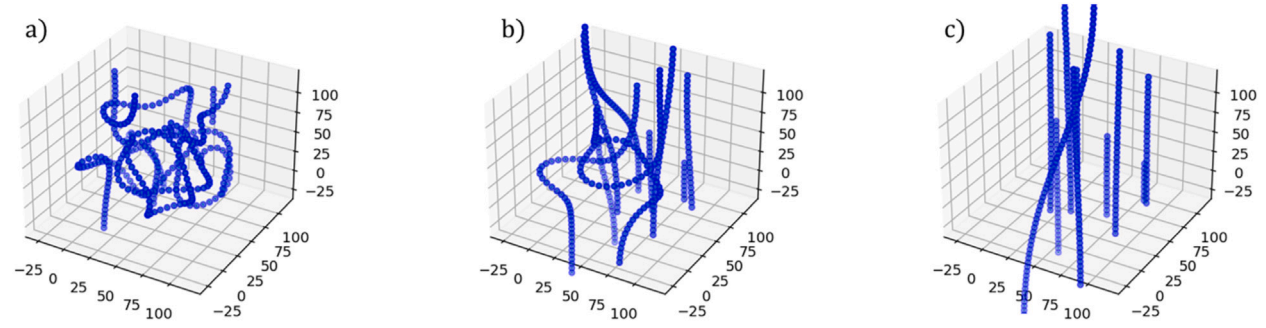


Fig. 7. Evolution of $N = 343$ NPs in the presence of a uniform external magnetic field of magnitude $B_{\text{ext}} = 100\,\text{mT}$ directed along the z axis. The initial condition (a) is an equilibrium without external field (see Fig. 5 at $t = 100\,\mu\text{s}$). The magnetic bonds are progressively destroyed (b), until the system is composed of an assembly of spears almost aligned along the external field (c). Captions at times $t = 0$, 50, and 100 μs. Space coordinates are expressed in nm.

4.1. Kinetic and potential energies in the stationary regime

To elucidate the relationship between thermal fluctuations and structural stability, multiple numerical simulations were performed across a range of temperatures, for a typical system consisting of nine NPs. The computational protocol is outlined as follows:

- For each simulation, the ambient temperature T is fixed, thereby setting the amplitude of the stochastic term, and the system is initialized in a linear spear-like configuration;
- Simulations are run and the mean kinetic energy is computed over successive time windows to identify the onset of thermodynamic equilibrium;
- Once equilibrium is established, extended simulations are conducted to determine the time-averaged kinetic and potential energies of the system. This phase lasts for a long time-scale (80 ms), to ensure that the overall structures are stable.
- For each temperature, the simulations are performed ten times with different randomized initial conditions, in order to reduce the statistical fluctuations. The observed standard deviation is less than 0.5 % for temperatures between $T = 0\,\text{K}$ and $T = 400\,\text{K}$, and less than 5 % for temperatures between $T = 400\,\text{K}$ and $T = 500\,\text{K}$.

The results from these simulations are presented in Fig. 9. We observe that the mean kinetic energy is directly proportional to the temperature, consistent with thermodynamic equilibrium. Specifically, one can verify the kinetic energy equipartition law: $E_K = \frac{D}{2} N k_B T$,

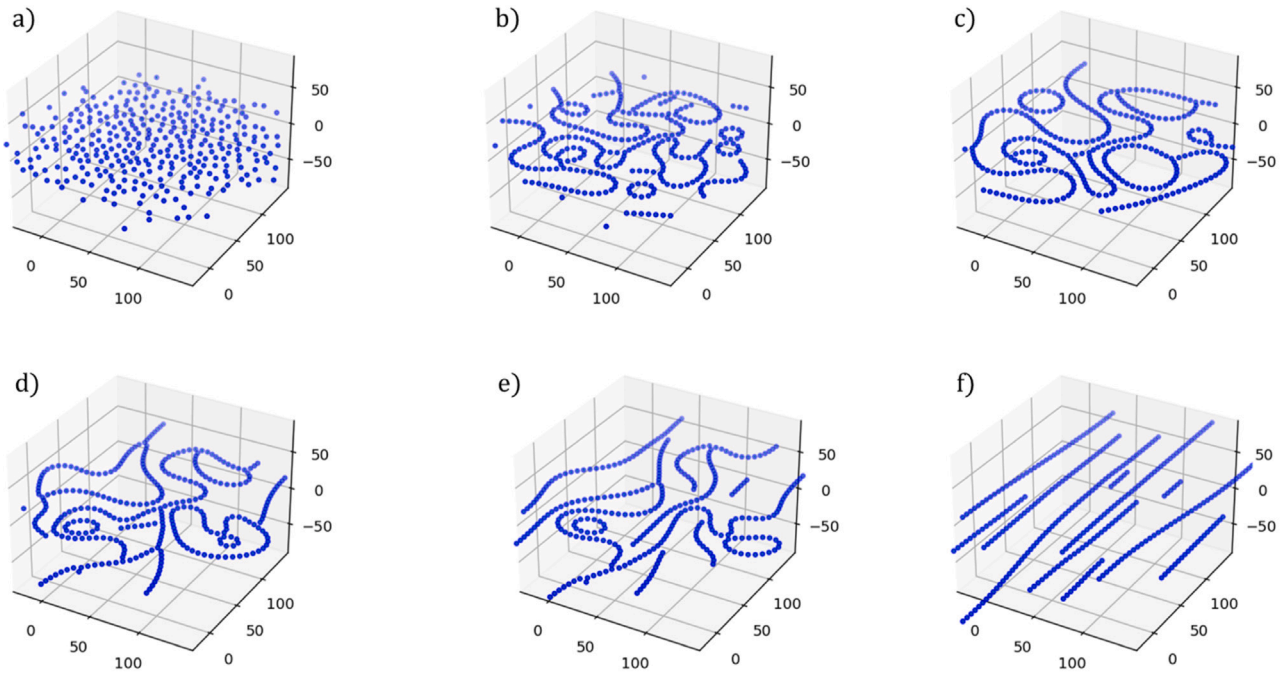


Fig. 8. Dynamics of $N = 324$ NPs at times $t = 0$, 10, 100, 110, 150 and 200 μs [figures (a) to (f), respectively]. The magnetic moment is free to rotate in 3D, but the positions of the NPs are constrained to remain in the plane $\{z = 0\}$. A uniform magnetic field parallel to the plane and with intensity 100 mT is added at $t = 100$ μs (c). Space coordinates are expressed in nm.

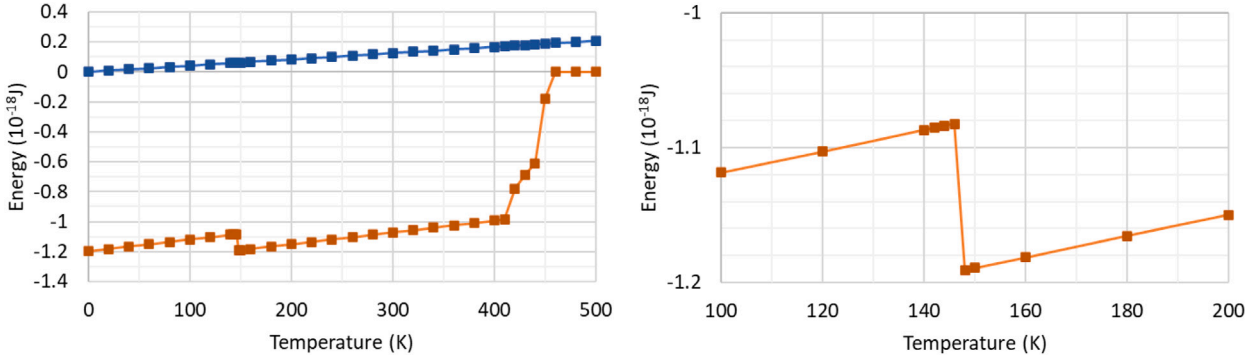


Fig. 9. System composed of nine NPs at thermodynamic equilibrium. Mean kinetic energy (dark blue) and mean potential energy (orange), in units of 10^{-18} J, plotted against the system temperature (a). Zoomed view of the potential energy curve near $T = 148$ K (b).

where $D = 6$ is the number of degrees of freedoms of each NPs (three positions and three Euler angles). One obtains: $E_K/T = 3Nk_B \approx 3.73 \times 10^{-22}$ J K^{-1}, which is very close to the value $E_K/T \approx 4 \times 10^{-22}$ J K^{-1} that can be deduced from the slope of the kinetic energy curve on Fig. 9(a). In contrast, the mean potential energy displays a more intricate dependence. It increases linearly from $T = 0$ K to $T = 146$ K, then displays a sharp decrease between $T = 146$ K and $T = 148$ K. It then grows again linearly (with roughly the same slope as before) from $T = 148$ K to $T = 420$ K. Another sharp transition occurs between $T = 420$ K and $T = 460$ K, followed by a plateau at zero potential energy.

Although the changes observed in the average potential energy clearly reveal two distinct temperature-induced structural transformations at $T \approx 146$ K and $T \approx 420$ K, the present data do not allow an unambiguous determination of their thermodynamic order. In particular, no sharp change of the average energy is observed within the numerical accuracy of our simulations. The first transition appears as an abrupt structural rearrangement from metastable spear-like structures toward energetically more favorable ring-like configurations [Fig. 9(b)], whereas the second transition corresponds to the progressive thermal evaporation of the magnetic assemblies. A rigorous characterization of these transitions would require finite-size scaling analyses together with the calculation of thermodynamic quantities such as the specific heat, susceptibility, or Binder cumulants. Such an investigation lies beyond the scope of the present study and will be addressed in future work.

4.2. Time evolution incorporating thermal effects

To achieve a more precise characterization of the NP system and its thermal stability, we conduct extended simulations over significantly longer time intervals (80 ms), well beyond the characteristic transition time to thermodynamic equilibrium. In particular, we investigate the temporal evolution near the transition temperatures observed in Fig. 9.

The forthcoming simulations (displayed in Figs. 10, 11 and 12) aim to describe the temporal dynamics of several system indicators, each averaged over a narrow time window to enhance readability:

- **Energy Indicators:** The graphs on the left column of Figs. 10–12 illustrate the evolution of the kinetic, potential, and total energies within the NP system;

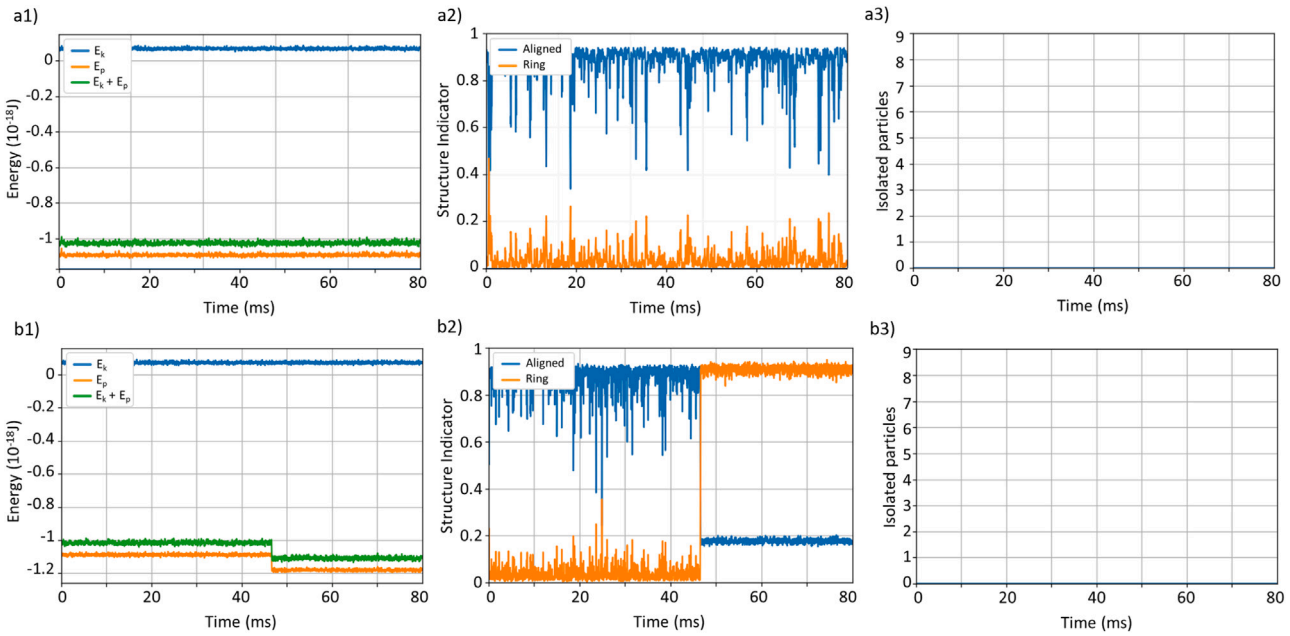


Fig. 10. Evolution of a system of $N = 9$ NPs at temperatures $T = 140\,\mathrm{K}$ (a) and $T = 148\,\mathrm{K}$ (b). Left column: kinetic, potential and total energies (respectively: blue, orange, and green curves) in units of $10^{-18}\,\mathrm{J}$; middle column: structural indicator of the presence of spears (blue curve) and rings (orange curve); right column: number of isolated particles.

- **Structural Indicators:** The middle-column graphs present the two statistical metrics introduced in Appendices B.1 and B.2, namely $\mathfrak{S}$ for the spear-like configuration and $\mathfrak{R}$ for the ring structure;
- **Isolation Indicator:** The right-column graphs track the number of isolated particles, defined as those lacking neighbors according to the criteria mentioned in Appendix B.3.

The initial condition for these simulations corresponds to the aligned spear configuration composed of nine magnetic NPs. This configuration is of particular interest due to its comparatively reduced stability relative to the ring structure, as will be evident from the simulation results discussed below.

In the next subsections, we focus on three regimes, corresponding to (i) the low-temperature transition near $T = 140\,\mathrm{K}$, (ii) the intermediate regime $150\,\mathrm{K} \lesssim T \lesssim 400\,\mathrm{K}$, and (iii) the high-temperature evaporation starting near $T = 410\,\mathrm{K}$.

4.2.1. Low-temperature transition

The low-temperature dynamics reveals how the system explores its energy landscape and how thermal fluctuations control access to competing basins of attraction. The two temperatures considered, $T = 140\,\mathrm{K}$ and $T = 148\,\mathrm{K}$, lie immediately below and above the sharp change observed in Fig. 9, and therefore probe the onset of the structural transition between the spear and ring configurations.

At $T = 140\,\mathrm{K}$ [Fig. 10(a)], the system remains confined within the basin of the spear configuration. The potential energy fluctuates only weakly around its equilibrium value ($\approx -1.2 \times 10^{-18}\,\mathrm{J}$), indicating that thermal agitation is insufficient to overcome the local barrier separating the spear from alternative minima. The structural indicators in Fig. 10(a2) oscillate around values characteristic of an aligned configuration, confirming that the system explores only the vicinity of this minimum. The absence of isolated particles [Fig. 10(a3)] shows that the connectivity structure of the assembly remains unchanged, with no major rearrangements. In summary, the dynamics corresponds to small-amplitude fluctuations within a single basin of attraction.

At $T = 148\,\mathrm{K}$ [Fig. 10(b)], the system acquires enough thermal energy to escape this basin. The structural indicators in Fig. 10(b2) exhibit a sharp, correlated transition near $t \approx 47\,\mathrm{ms}$: the spear indicator collapses while the ring indicator rises, signaling a rapid crossing of the energy barrier. Thermal agitation bends the spear sufficiently for its extremities to approach, and magnetic-dipole forces then stabilize a new bond, closing the structure into a ring.

The potential energy evolution [Fig. 10(b1)] quantifies this process. Before the transition, the system fluctuates around $-1.08 \times 10^{-18}\,\mathrm{J}$, consistent with the spear configuration. After the transition, the energy drops to $-1.18 \times 10^{-18}\,\mathrm{J}$, reflecting the formation of an additional dipolar bond. The energetic gain $\Delta E_p = 10^{-19}\,\mathrm{J}$ ($\Delta E_p/k_B = 7243\,\mathrm{K}$) translates into a gain $\Delta E_p/(N\,D)$ per particle ($N = 9$) and per degree of freedom ($D = 6$). In temperature units, this yields $7243/54 \approx 134\,\mathrm{K}$, in qualitatively good agreement with the observed transition temperature. This is consistent with the transition being thermally activated and governed by the interplay between dipolar attraction and configurational entropy.

Throughout the dynamics no particles become isolated, as shown in Fig. 10(b3), indicating that the transition preserves global structural coherence. The system therefore undergoes a collective reorganization rather than a fragmentation process.

4.2.2. Intermediate temperature regime

The study of the system at a temperature of $T = 300\,\mathrm{K}$, as illustrated in Fig. 11(a), is particularly insightful because it captures an intermediate regime well removed from both the structural transitions at $T = 146$–$148\,\mathrm{K}$ and $T = 420$–$460\,\mathrm{K}$.

The primary observation from Fig. 11(a2) is that, although the initial configuration is a spear, the system almost instantaneously converges toward the basin of attraction associated with the ring structure (the convergence is so fast as to be barely visible on the figure). Prior results at $T = 148\,\mathrm{K}$ (see Section 4.2.1) established that the ring possesses a lower potential energy than the spear. The current simulation at $T = 300\,\mathrm{K}$ further demonstrates that the ring is significantly more thermodynamically stable, with a deeper basin of attraction. This enhanced stability is also evident in the low-amplitude fluctuations of the structural indicator around its mean value [Fig. 11(a2)] – compared to the large fluctuations observed at $T = 140\,\mathrm{K}$ [Fig. 10(a2)] – suggesting

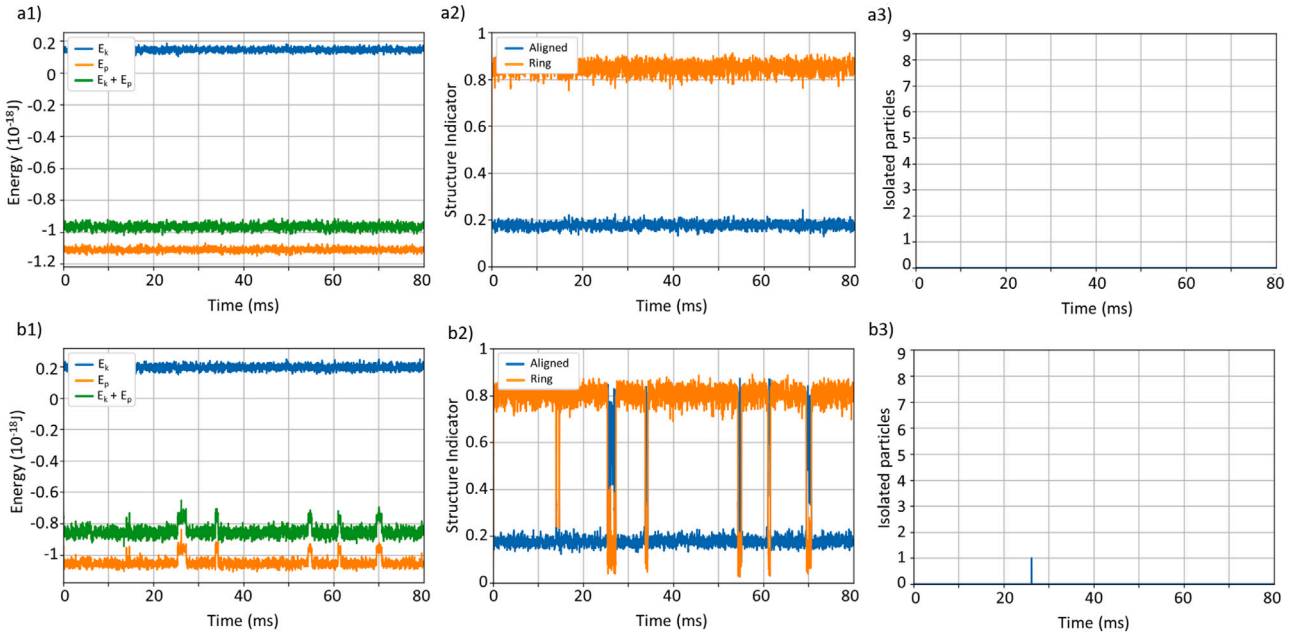


Fig. 11. Evolution of a system of $N = 9$ NPs at temperatures $T = 300\,\mathrm{K}$ (a) and $T = 410\,\mathrm{K}$ (b). Left column: kinetic, potential and total energies (respectively: blue, orange, and green curves) in units of $10^{-18}\,\mathrm{J}$; middle column: structural indicator of the presence of spears (blue curve) and rings (orange curve); right column: number of isolated particles.

that the configuration remains tightly bound to the ring structure with minimal deviations.

To reinforce this conclusion, additional simulations were performed at $T = 300\,\mathrm{K}$ using different initial configurations. Provided that the initial inter-particle distances were not excessively large (so that structural transformations could be observed within the simulation timescale), all trajectories invariably converged to the ring configuration. These findings strongly suggest that the ring acts as a global attractor for the system's dynamics at intermediate temperatures.

4.2.3. High-temperature evaporation

The high-temperature regime is governed by the competition between thermal agitation and dipolar magnetic cohesion. As temperature increases, thermal fluctuations progressively overcome the energy barriers associated with magnetic bonding, driving the system from reversible structural fluctuations to irreversible fragmentation and finally to complete vaporization.

At $T = 410\,\mathrm{K}$ [Fig. 11(b)], the system reaches the onset of the high-temperature transition (Fig. 9). Thermal energy becomes sufficient to sporadically disrupt individual magnetic bonds, producing intermittent transitions between ring and spear configurations [Fig. 11(b2)]. These transitions are reflected by abrupt potential-energy variations of order $10^{-19}\,\mathrm{J}$ [Fig. 11(b1)]. A brief detachment event occurs near $t \approx 26\,\mathrm{ms}$ [Fig. 11(b3)], during which a NP becomes isolated from the rest of the structure, coinciding with a peak in potential energy. The mechanism involves sequential rupture of two bonds: first a bond within the ring, forcing the system into a spear configuration, then a second rupture at a spear extremity, where particles are weakly bound due to larger inter-particle distances. At this stage, evaporation is rare but dynamically accessible.

At $T = 440\,\mathrm{K}$ [Fig. 12(a)], evaporation becomes statistically favored. Thermal agitation is now strong enough to break both magnetic bonds of individual particles, enabling them to detach from the structure. Because dipolar forces decay as r^{-4}, detached particles rapidly exit the interaction range and follow nearly free Brownian motion. The number of isolated particles increases steadily [Fig. 12(a3)], with occasional reattachments producing small oscillations. Structural indicators computed on the largest connected component [Fig. 12(a2)] show accelerated fluctuations, reflecting the decreasing structural stability. Detachments occur almost exclusively during spear-like intervals, consistent with the lower robustness of spear configurations relative to rings. Energetic signatures remain clear: each detachment produces a sharp increase in potential energy, while reformation of a bond yields a corresponding decrease [Fig. 12(a1)].

At $T = 470\,\mathrm{K}$ [Fig. 12(b)], the system reaches the final stage of the transition: rapid and complete vaporization. All magnetic bonds break within a few tens of milliseconds, and the potential energy approaches zero as the assembly becomes a gas of isolated NPs undergoing free Brownian motion. After $t \gtrsim 40\,\mathrm{ms}$, all particles are isolated, the connectivity indicator reaches its maximum allowed value $N = 9$, and the spear and ring indicators drop to zero. Throughout this regime, sharp changes in the potential energy remain reliable markers of structural transitions and particle escape events.

Further, Fig. 12(b) emphasizes the relative stability properties of the ring and spear configurations during the vaporization process. Indeed, particle detachment events almost exclusively occur when the system adopts a spear-like structure. The structural indicators lose reliability after $t = 20\,\mathrm{ms}$, when rapid vaporization begins; however, prior to this moment, all particle ejection events are associated with the spear configuration.

5. Application to a real-life solvent: 1-Octadecene

In Section 4, we considered a system of magnetic NPs immersed in a highly idealized fluid that neither freezes nor boils, and whose viscosity remains constant ($0.5\,\mathrm{mPa\,s}$), independent of temperature.

Here, we turn our attention to a more realistic scenario where the NPs are immersed in 1-octadecene, which is commonly employed as a high-boiling, non-coordinating solvent in the thermal decomposition synthesis of magnetic NPs, particularly iron [42] and cobalt [43] oxide nanocrystals. Its elevated boiling point ($\approx 315\,^{\circ}\mathrm{C}$) allows reactions to be conducted at high temperatures with precise thermal control, which is critical for promoting controlled nucleation, uniform particle growth, and high crystallinity. Due to its chemically inert and weakly coordinating nature, 1-octadecene does not significantly interact with the

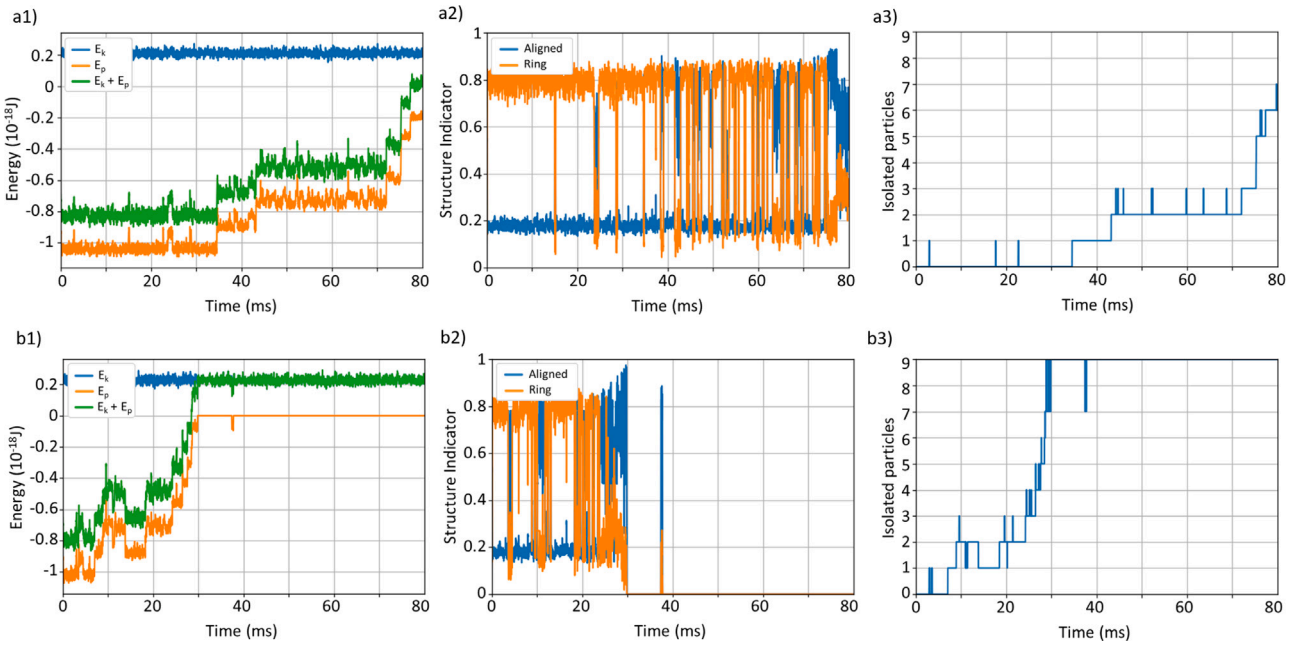


Fig. 12. Evolution of a system of $N = 9$ NPs at temperatures $T = 440\,\mathrm{K}$ (a) and $T = 470\,\mathrm{K}$ (b). Left column: kinetic, potential and total energies (respectively: blue, orange, and green curves) in units of 10^{-18} J; middle column: structural indicator of the presence of spears (blue curve) and rings (orange curve); right column: number of isolated particles.

Table 1
Dynamic viscosity of 1-octadecene for several temperatures.
Source: Values taken from Ref. [48]

$T = 410$ K	$T = 440$ K	$T = 470$ K	$T = 510$ K
$\eta = 0.60$ mPa s	$\eta = 0.45$ mPa s	$\eta = 0.33$ mPa s	$\eta = 0.24$ mPa s

NP surface, thereby enabling surface-active ligands such as oleic acid and oleylamine to govern particle growth kinetics and size distribution. Consequently, the use of 1-octadecene facilitates the reproducible synthesis of monodisperse magnetic NPs with well-defined morphologies and tunable dimensions [44–47]. The dynamic viscosity values of 1-octadecene as a function of temperature are taken from the Ref. [48] and were obtained using the Joback method. Although the forthcoming simulations will employ 1-octadecene as the solvent, other options are also of interest. In particular, squalane is frequently used for the synthesis of magnetic iron-oxide spinel nanoparticles [49,50], owing to its very high boiling point (≈610 °C [51]).

1-Octadecene is liquid in the range of temperatures that are of interest for us (the melting and boiling points at atmospheric pressure are, respectively, 287 K and 588 K). We thus performed 4 additional simulations with temperatures ranging from 410 K to 510 K. The viscosity of 1-octadecene for these temperatures is shown in Table 1.

The numerical simulations follow the same procedure as detailed in Section 4.1. The results for a system of 9 NPs immersed in 1-octadecene are shown in Fig. 13, and closely resemble those obtained in the case of an idealized solvent, see Section 4.2.

At $T = 410\,\mathrm{K}$, the thermal agitation is insufficient to disrupt the structures present in the system. No isolated NPs are observed, and all 9 particles remain organized in a ring configuration. However, brief intervals occur during which the ring structure indicator temporarily drops, see Fig. 13(a2), corresponding to the transient breaking of a magnetic bond. Each such event coincides with a small energy peak [Fig. 13(a1)]. Qualitatively, the system appears less agitated than in the previous simulation at $T = 410\,\mathrm{K}$ [Fig. 11(b)], likely due to the higher viscosity of the solvent.

At $T = 440\,\mathrm{K}$, the system exhibits an evaporation phenomenon, observable in Fig. 13(b). After sufficient kinetic energy has been accumulated by a ring structure, it can escape its local energy minimum, resulting in the breaking of magnetic bonds between particles. For instance, at $t = 43$ ms, the ring transforms into an aligned configuration (spear), as evidenced by the drop in the ring structure indicator in Fig. 13(b2) and a corresponding increase in the spear structure indicator. A particle at one extremity is ejected from the structure and becomes isolated [Fig. 13(b3)], while the remaining particles revert to the ring configuration. This process repeats until all NPs are ejected, leaving them isolated by the end of the simulation.

At $T = 470$ and $T = 510$ K, see Fig. 13(c), the same evaporation phenomenon is observed, but the rate of structural disintegration into isolated NPs increases with temperature. No significant influence of viscosity variations is observed in these cases.

6. Conclusion

This study presents a detailed numerical investigation of the self-organization of monodomain magnetic NPs suspended in a viscous fluid, governed primarily by dipolar magnetic interactions and dissipative viscous forces. Through molecular dynamics simulations, we reveal how system complexity evolves as a function of particle number, thermal agitation, external magnetic fields, and spatial confinement. A central contribution of our work is the introduction of robust statistical estimators for spear and ring configurations, enabling quantitative assessment of structural evolution and stability.

In the absence of thermal fluctuations, the system converges toward equilibrium structures characterized by energetically favorable configurations. For small particle numbers N, the NPs predominantly form spear-like and ring-like structures. As the number of particles increases, these simple configurations give way to more intricate filamentous aggregates, with triple points serving as key junctions. A statistical analysis across thousands of realizations quantifies this structural transition and confirms the disappearance of simple patterns in favor of increasingly complex assemblies for large N. We note that the present simulations keep the NP concentration approximately constant when

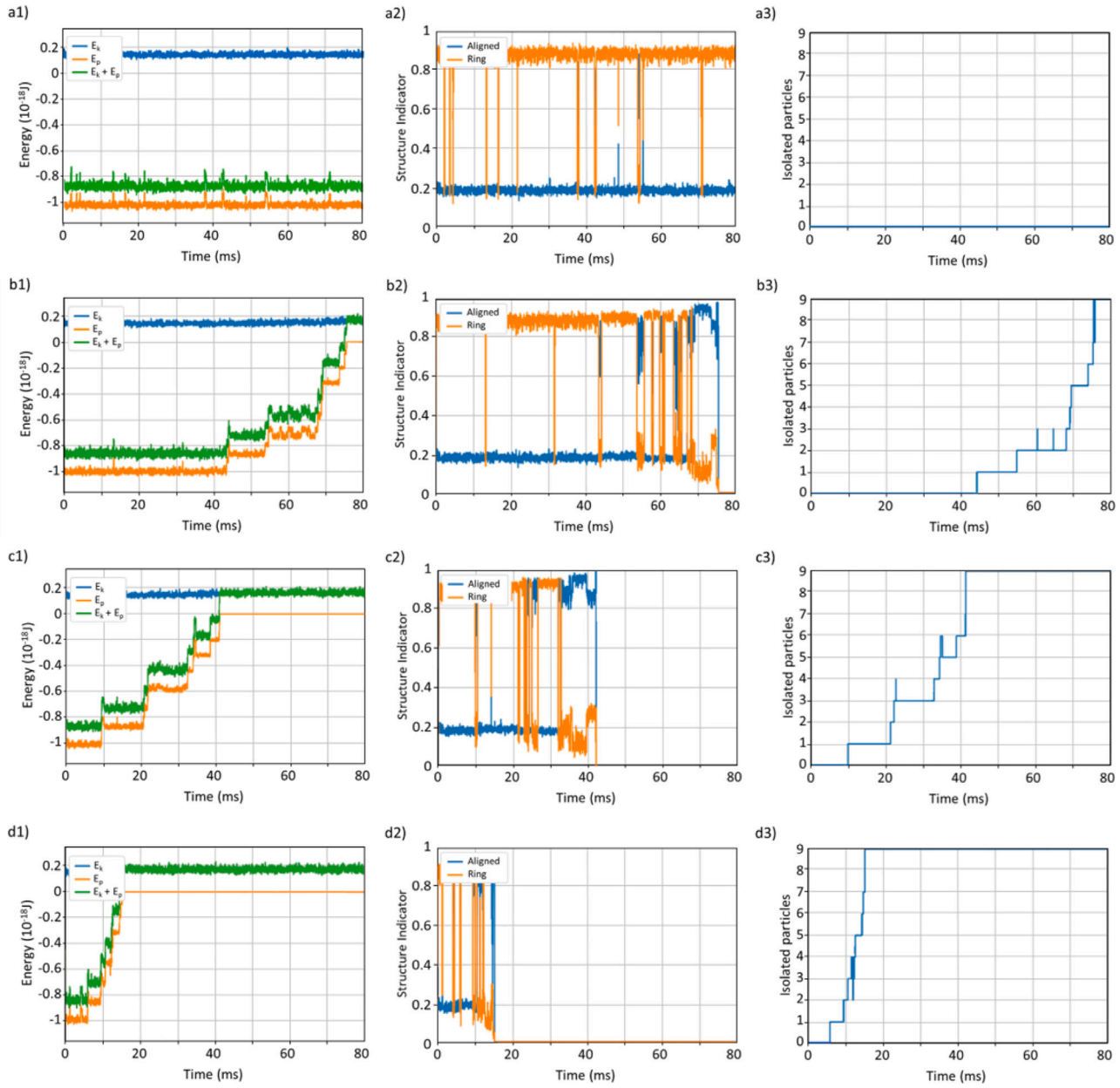


Fig. 13. Evolution of a system of $N = 9$ NPs immersed in 1-octadecene, at temperatures $T = 410\,\mathrm{K}$ (a), $T = 440\,\mathrm{K}$ (b), $T = 470\,\mathrm{K}$ (c), and $T = 510\,\mathrm{K}$ (d). Left column: kinetic, potential and total energies (respectively: blue, orange, and green curves) in units of $10^{-18}\,\mathrm{J}$; middle column: structural indicator of the presence of spears (blue curve) and rings (orange curve); right column: number of isolated particles.

varying N. Therefore, concentration and number of NPs in a given aggregate constitute related but distinct control parameters, and only the latter was investigated here. A systematic study varying these parameters independently would provide a useful test of the present predictions. Additional simulations demonstrated the impact of external magnetic fields, which reorient and simplify complex aggregates into aligned spear-like formations. Confinement to 2D geometries further enhances structural observability and confirms the persistence of filamentous self-assembly under planar constraints.

Thermal fluctuations introduce dynamic restructuring behavior, with structural transitions characterized by variations in potential energy and magnetic bond stability. We first studied thermal effects in the case of an ideal solvent with temperature-independent viscosity of the same order as that of water at 330 K. For this idealized scenario, we identified a critical regime near $T \approx 148\,\mathrm{K}$, where spear structures transition into ring configurations, and another at $T \approx 420$–$460\,\mathrm{K}$, beyond which magnetic cohesion is lost and vaporization-like dispersal occurs. These transitions are accompanied by measurable energetic signatures and shifts in structural indicators. Importantly, we have identified three different time scales for the NP evolution: (i) it takes about 100 ns for two NPs, initially at a distance comparable to their radius R, to undergo a collision (Figs. 1, 2, and 3); (ii) it takes about 10 µs for a filament to travel a distance of the order of R (Fig. 5); and finally (iii) it takes about 1 ms for a filament to break under the action of thermal agitation (Figs. 10, 11 and 12). Each of the above time scales are separated by a factor 100, making their numerical simulation a particularly hard task. Such results were largely confirmed for a realistic scenario where the solvent's viscosity depends on the temperature. In our simulations, we employed 1-octadecene as the solvent, which is a common choice for the synthesis of magnetic NPs.

Although the present study is theoretical and computational, its predictions are directly amenable to experimental verification. The use of

cobalt NPs dispersed in 1-octadecene closely follows standard synthesis routes employed for magnetic nanocolloids. The predicted evolution from chains and rings toward filamentary structures containing triple junctions could be investigated by transmission electron microscopy (TEM) or cryogenic TEM techniques that have already enabled the direct visualization of dipolar magnetic assemblies [31,52]. Likewise, recent developments in liquid-cell TEM make it possible to monitor the dynamics of NP self-assembly under *in situ* conditions [53], opening the way to experimental investigations of the temperature-induced structural transitions predicted in this work. Finally, the influence of external magnetic fields on the aggregate morphology could be characterized by *in situ* magnetic imaging techniques such as magnetic force microscopy. We hope that the present work will stimulate such experimental studies and provide a quantitative framework for interpreting the self-organization dynamics of dipolar magnetic NPs.

On the theory front, an interesting perspective will be to investigate in detail the various structural transitions and their nature (first or second order) in larger NP systems. Around the high-temperature transition associated with vaporization, fission and multifragmentation processes may occur. Such phenomena have been observed at other physical time and spatial scales, notably in highly excited nuclei and atomic clusters. It has been demonstrated through statistical methods that a hot nucleus [54] or a hot atomic cluster [55] tends to fragment into two or more intermediate-sized nuclei or clusters rather than dissipating excess energy through the evaporation of single particles (a neutron or an atom). Such studies will require the development of alternative estimators. Furthermore, it would be worthwhile to explore how the critical temperature and associated latent heat evolve with the number of NPs and their properties (e.g., material and size), as well as with the properties of the solvent (e.g., its viscosity).

In summary, the present results provide valuable insight into the organizing principles of dipolar NP systems and set the stage for future experimental validation and the development of controlled NP assembly strategies. They also underline the universal nature of fragmentation and reorganization phenomena at very different spatial scales, ranging from nuclei (10^{-15} m) and metal clusters (10^{-9} m), up to the NP aggregates considered in the present work (10^{-8} m).

CRediT authorship contribution statement

Ludovic Godard-Cadillac: Writing – review & editing, Writing – original draft, Validation, Software, Methodology, Investigation, Conceptualization. **Paul-Antoine Hervieux:** Writing – review & editing, Methodology, Investigation, Conceptualization. **Giovanni Manfredi:** Writing – review & editing, Writing – original draft, Methodology, Investigation, Conceptualization.

Declaration of competing interest

The authors declare that they have no known competing financial interests or personal relationships that could have appeared to influence the work reported in this paper.

Acknowledgments

The authors acknowledge financial support by the ANR project MOSICOF ANR-21-CE40-0004 (Modeling and Simulation of Complex Ferromagnetic Systems). We thank Constantin Doru, Damien Mertz, Matthias Pauly, and Antonio Stocco for useful discussions.

Appendix A. Numerical solution of the dynamical equations

A.1. Numerical integration of the differential equations

We have a system of ODEs which are second-order for the evolution of the positions $\boldsymbol{x}_i \in \mathbb{R}^3$ and first-order for the evolution of the angular velocity $\boldsymbol{\omega}_i \in \mathbb{R}^3$ and the magnetic moment $\boldsymbol{m}_i \in \mathbb{S}^2$. We construct our numerical method using a splitting technique based on the Velocity-Verlet integration (for the second-order equations) and the Heun's method (for the first-order equations). We recall here the basic tenants of these two numerical methods for a generic variable $\boldsymbol{x}(t)$ and its velocity $\boldsymbol{v} = \dot{\boldsymbol{x}}$ (the overdot denotes differentiation with respect to the time t) from which are constructed the algorithm implemented for this article:

Velocity-Verlet integration for second-order dissipative equations $\ddot{\boldsymbol{x}}(t) = \boldsymbol{\mathcal{F}}\big(\boldsymbol{x}(t)\big) - \lambda\dot{\boldsymbol{x}}$:

- Calculate the new position: $\boldsymbol{x}(t+\Delta t) = \boldsymbol{x}(t) + \boldsymbol{v}(t)\Delta t + \frac{1}{2}\boldsymbol{a}(t)\Delta t^2$,
- Derive the new acceleration from the interaction potential: $\boldsymbol{a}(t+\Delta t) = \mathcal{F}\big(\boldsymbol{x}(t+\Delta t)\big)$,
- Calculate the new velocity: $\boldsymbol{v}(t+\Delta t) = \boldsymbol{v}(t) + \frac{1}{2}\Big(\boldsymbol{a}(t+\Delta t) + \boldsymbol{a}(t)\Big)\Delta t - \frac{\lambda}{2}\Big(\boldsymbol{v}(t+\Delta t) + \boldsymbol{v}(t)\Big)\Delta t$.

Heun's method for first order differential equations $\dot{\boldsymbol{x}}(t) = \mathcal{F}\big(\boldsymbol{x}(t)\big)$:

- Calculate a predictor $\widetilde{\boldsymbol{x}}(t+\Delta t) = \boldsymbol{x}(t) + \mathcal{F}\big(\boldsymbol{x}(t)\big)\Delta t$,
- Calculate a corrector $\widehat{\boldsymbol{x}}(t+\Delta t) = \boldsymbol{x}(t) + \mathcal{F}\big(\widetilde{\boldsymbol{x}}(t)\big)\Delta t$,
- Take the average $\boldsymbol{x}(t+\Delta t) = \frac{1}{2}\Big(\widetilde{\boldsymbol{x}}(t+\Delta t) + \widehat{\boldsymbol{x}}(t+\Delta t)\Big)$.

The simplicity of these methods, their stability and their good order of convergence have made these methods very popular. One weakness of Velocity-Verlet method is that the computation of $\boldsymbol{a}(t+\Delta t)$ should not require the knowledge of $\boldsymbol{v}(t+\Delta t)$, which is not our case here (due to the dissipation term, which is proportional to the velocity). Nevertheless, it is possible to overcome this problem by computing an approximation of $\boldsymbol{v}(t+\Delta t)$.

To hybridize the Velocity-Verlet and Heun methods, we use an approach inspired from standard splitting schemes. Using the notations introduced in Eqs. (1), (2) and (7), the Heun-Verlet algorithm for our problem reads as follows:

- First step of the Heun's method: compute a predictor of the angular velocity and magnetic moment (for all i):

$$\widetilde{\boldsymbol{\omega}_i}(t+\Delta t) = \boldsymbol{\omega}_i(t) + \frac{\Delta t}{I}\Big(\boldsymbol{T}_i(t)\ \Big) - \zeta_r\boldsymbol{\omega}(t)\Big),$$
$$\widetilde{\boldsymbol{m}_i}(t+\Delta t) = \boldsymbol{m}_i(t) + \Delta t\Big(\boldsymbol{m}_i(t)\times B_i(t)\Big);$$

- First step of the Velocity-Verlet algorithm:

$$\boldsymbol{x}_i(t+\Delta t) = \boldsymbol{x}_i(t) + \Delta t\,\boldsymbol{v}_i(t) + \frac{\Delta t^2}{m}\Big(\boldsymbol{F}_i(t) - \zeta_t\,\boldsymbol{v}_i(t)\Big);$$

- Define the conservative forces $\widetilde{\boldsymbol{F}_i}(t+\Delta t)$ and torques $\widetilde{\boldsymbol{T}_i}(t+\Delta t)$ associated to the above guesses. They are computed with Eqs. (3), (4), and (5), using $\widetilde{\boldsymbol{\omega}_j}(t+\Delta t)$ and $\widetilde{\boldsymbol{m}_j}(t+\Delta t)$, together with the new positions $\boldsymbol{x}_j(t+\Delta t)$;
- Second step of the Heun's method:

$$\widehat{\boldsymbol{\omega}_\boldsymbol{i}}(t+\Delta t) = \boldsymbol{\omega}_i(t) + \frac{\Delta t}{I}\Big(\widetilde{\boldsymbol{T}_i}(t+\Delta t) - \zeta_r\widetilde{\boldsymbol{\omega}_i}(t)\Big),$$
$$\widehat{\boldsymbol{m}_i}(t+\Delta t) = \boldsymbol{m}_i(t) + \Delta t\Big(\widetilde{\boldsymbol{m}_i}(t)\times\widetilde{\boldsymbol{B}_i}(t)\Big);$$

- Third step of the Heun's method:

$$\boldsymbol{\omega}_i(t+\Delta t) = \frac{1}{2}\Big(\widetilde{\boldsymbol{\omega}_i}(t+\Delta t) + \widehat{\boldsymbol{\omega}_i}(t+\Delta t)\Big),$$
$$\boldsymbol{m}_i(t+\Delta t) = \frac{1}{2}\Big(\widetilde{\boldsymbol{m}_i}(t+\Delta t) + \widehat{\boldsymbol{m}_i}(t+\Delta t)\Big);$$

- Second step of the Velocity-Verlet algorithm: we compute $\boldsymbol{F}_i(t+\Delta t)$ and $\boldsymbol{T}_i(t+\Delta t)$ using $\boldsymbol{\omega}_j(t+\Delta t)$, $\boldsymbol{m}_j(t+\Delta t)$ and $\boldsymbol{x}_j(t+\Delta t)$;
- Third step of the Velocity-Verlet algorithm:

$$\boldsymbol{v}_i(t+\Delta t) = \boldsymbol{v}_i(t) + \frac{\Delta t}{2\mu}\left[\Big(\boldsymbol{F}_i(t+\Delta t) - \zeta_t\,\boldsymbol{v}_i(t+\Delta t)\Big) - \Big(\boldsymbol{F}_i(t) - \zeta_t\,\boldsymbol{v}_i(t)\Big)\right].$$

- To ensure that the constraint $|m_i(t)|^2 = |m_i(0)|^2$ is preserved by the algorithm, we eventually proceed to a projection of the magnetic vector on the sphere.

Note that it would be less precise to integrate separately the first- and second-order equations, since the second step of Heun's method requires the knowledge of $\boldsymbol{x}_i(t+\Delta t)$, while we need $\boldsymbol{m}_i(t+\Delta_t)$ before the last step of Velocity Verlet.

A.2. Simulation of thermal effects with white noise

In the presence of temperature, a white-noise term is added to the equations and this white noise is added in the standard numerical scheme (for an introduction to simulations with noise and numerical integration of stochastic differential equations, we refer to [56,57]). In the presence of Gaussian white noise $\mathrm{d}\boldsymbol{W}_t$ which covariant matrix is the diagonal matrix of coefficients σ^2, the algorithms presented above requires to be modified to take into account these random effects. The splitting scheme presented for our problem is also modified accordingly.

In our model, the dynamics of the NP centers is given by:

$$\mathrm{d}\boldsymbol{x}_i = \boldsymbol{v}_i\,\mathrm{d}t, \qquad \text{and} \qquad m\,\mathrm{d}\boldsymbol{v}_i = \boldsymbol{F}_i\big(\boldsymbol{x}_i(t)\big)\,\mathrm{d}t - \zeta^{tr}\boldsymbol{v}_i\,\mathrm{d}t + \sqrt{2k_BT\zeta^{tr}}\,\mathrm{d}\boldsymbol{W}_i,$$

where $\boldsymbol{F}_i$ denotes the sum of the conservative forces (magnetic and repulsive). The equation for the rotation of the NPs is also modified accordingly:

$$I\,\mathrm{d}\boldsymbol{\omega}_i = \boldsymbol{m}_i \times \boldsymbol{B}_i\,\mathrm{d}t - \zeta^r\boldsymbol{\omega}_i\,\mathrm{d}t + \sqrt{2k_BT\zeta^r}\,\mathrm{d}\widetilde{\boldsymbol{W}}_i, \qquad \text{and} \qquad \mathrm{d}\boldsymbol{m}_i = \boldsymbol{\omega}_i \times \boldsymbol{m}_i\,\mathrm{d}t,$$

where $\boldsymbol{W}_i$ and $\widetilde{\boldsymbol{W}}_i$ denote centered, normalized white-noise processes, independent of one another for all times, and independent of $\boldsymbol{W}_j$ and $\widetilde{\boldsymbol{W}}_j$ for any index $j \neq i$.

The modified Heun and Velocity Verlet integrators used in this work are formulated, in complete mathematical generality, as follows:

Stochastic Heun's method for first order equations of the form $\mathrm{d}\boldsymbol{\omega}(t) = \mathcal{F}\big(\boldsymbol{\omega}(t)\big)\mathrm{d}t + \sigma\mathrm{d}\boldsymbol{W}_t$:

- Calculate a predictor $\widetilde{\boldsymbol{\omega}}(t+\Delta t) = \boldsymbol{\omega}(t) + \mathcal{F}\big(\boldsymbol{\omega}(t)\big)\Delta t$,
- Calculate a corrector $\widehat{\boldsymbol{\omega}}(t+\Delta t) = \boldsymbol{\omega}(t) + \mathcal{F}\big(\widetilde{\boldsymbol{\omega}}(t)\big)\Delta t$,
- Take the average and add noise : $\boldsymbol{\omega}(t+\Delta t) = \frac{1}{2}\Big(\widetilde{\boldsymbol{\omega}}(t+\Delta t) + \widehat{\boldsymbol{\omega}}(t+\Delta t)\Big) + \sqrt{\sigma^2\Delta t}\,\boldsymbol{W}(t+\Delta t)$.

In the expression above, the term $\boldsymbol{W}(t)$ denotes a realization of the standard white noise $\mathrm{d}\boldsymbol{W}_t$ which increment follows a centered reduced normal law $\mathcal{N}(0,1)$.

Stochastic Velocity-Verlet integration for second-order dissipative equations with noise $\mathrm{d}\dot{\boldsymbol{x}}(t) = \boldsymbol{\mathcal{F}}\big(\boldsymbol{x}(t)\big)\mathrm{d}t - \lambda\dot{\boldsymbol{x}}\mathrm{d}t + \sigma\mathrm{d}\boldsymbol{W}_t$:

- Calculate the new position: $\boldsymbol{x}(t+\Delta t) = \boldsymbol{x}(t) + \boldsymbol{v}(t)\Delta t + \frac{1}{2}\boldsymbol{a}(t)\Delta t^2$,
- Derive the new acceleration from the interaction potential: $\boldsymbol{a}(t+\Delta t) = \mathcal{F}\big(\boldsymbol{x}(t+\Delta t)\big)$,
- Calculate the new velocity and add noise :

$$\boldsymbol{v}(t+\Delta t) = \boldsymbol{v}(t) + \frac{1}{2}\Big(\boldsymbol{a}(t+\Delta t) + \boldsymbol{a}(t)\Big)\Delta t - \frac{\lambda}{2}\Big(\boldsymbol{v}(t+\Delta t) + \boldsymbol{v}(t)\Big)\Delta t + \sqrt{\sigma^2\Delta t}\,\boldsymbol{W}(t+\Delta t).$$

A.3. Generation of the initial conditions

A central methodological issue concerns the choice of the initial conditions for the simulations presented in this work. Difficulties may arise when the NPs are either too close to one another or excessively far apart. If two particles are initialized at an insufficient separation, the simulation becomes numerically unstable and may blow up; conversely, a particle placed too far from the others effectively behaves as if it were absent from the system.

To address this issue, we rely on the thermal component of the numerical model and make use of the thermalization time. The particles are first positioned on a regular grid with spacing equal to their diameter. The simulation is then run with only thermal fluctuations and the repulsive potential activated, while magnetic interactions are switched off. A strong confining potential is added to prevent particles from leaving a sphere of prescribed radius $R_{\max}$.

Thermalization is reached after a short number of iterations, with the velocity distribution satisfying a Maxwell–Boltzmann law. The thermalization time is estimated once and subsequently reused. The radius $R_{\max}$ is chosen proportional to $\sqrt[3]{N}$ with the proportionality constant determined empirically so as to avoid configurations in which particles are initially isolated (i.e., separated from all others by more than ten diameters). The configuration obtained at the end of this thermalization stage is used as the initial condition for the full simulation. This preliminary step was performed prior to each of the simulations leading to the statistical results shown in Fig. 6.

Appendix B. Statistical estimators

To quantitatively assess the prevalence of spear or ring configurations in long-time simulations – once all kinetic energy has been dissipated via viscous interactions with the fluid – we introduce two statistical estimators tailored to characterize such structures.

B.1. Spears

To measure how far a given structure of nano-particles $(\boldsymbol{x}_1, \boldsymbol{m}_1), \dots, (\boldsymbol{x}_N, \boldsymbol{m}_N) \in \mathbb{R}^3 \times \mathbb{S}^2$ is from a "spear" structure, we proceed as follows:

1. We compute the average position of the NPs and the associated variance:

$$\overline{\boldsymbol{x}} = \frac{1}{N}\sum_{i=1}^{N}\boldsymbol{x}_i, \quad \text{and} \quad \sigma^2 = \frac{1}{N-1}\sum_{i=1}^{N}|\boldsymbol{x}_i - \overline{\boldsymbol{x}}|^2.$$

2. We solve a least-square linear regression problem for the positions $\boldsymbol{x}_1, \dots, \boldsymbol{x}_N$ with respect to a line. This consists in finding $\overline{\boldsymbol{u}} \in \mathbb{S}^2$ a solution of the following minimization problem:

$$\min_{\boldsymbol{u}\in\mathbb{S}^2}\sum_{i=1}^{N}\mathrm{dist}\big(\boldsymbol{x}_i; \overline{\boldsymbol{x}} + \boldsymbol{u}\mathbb{R}\big)^2,$$

where the distance between a point and a set is given by $\mathrm{dist}(\boldsymbol{x}; A) = \inf_{\boldsymbol{y}\in A}|\boldsymbol{x} - \boldsymbol{y}|$.

3. From this regression, we introduce the residual variance, which is the variance in the data that is not explained by the regression:

$$\sigma_\ell^2 = \frac{1}{N-1}\sum_{i=1}^{N}|\boldsymbol{x}_i - P_\ell\boldsymbol{x}_i|^2,$$

where P_ℓ designates the orthogonal projection on the optimal line $\overline{\boldsymbol{x}} + \overline{\boldsymbol{u}}\mathbb{R}$.

4. There remains to check whether the magnetic moments are aligned with the structure. For that purpose, we compute the mean scalar product between the magnetic moments and the main direction of the structure $\overline{\boldsymbol{u}}$ (assuming that $|\boldsymbol{m}| = 1$):

$$S_\ell = \overline{\boldsymbol{u}} \cdot \frac{1}{N}\sum_{i=1}^{N}\boldsymbol{m}_i$$

5. We introduce the spear estimator:

$$\mathfrak{S} = \left(1 - \frac{\sigma_\ell^2}{\sigma^2}\right) S_\ell^2, \quad \mathfrak{S} \in [0, 1].$$

This metric reaches its maximum value when particles are perfectly aligned along a line and their magnetic moments are collinear and uniformly oriented. The term $1 - \sigma_\ell^2/\sigma^2$ corresponds to the classical coefficient of determination in regression analysis, while $S_\ell = \pm 1$ indicates complete magnetic moment alignment with $\overline{\boldsymbol{u}}$.

B.2. Rings

Analogously, we construct an estimator to assess the proximity of a configuration to a ring-like geometry:

1. We solve a least-square linear regression problem for the positions $\boldsymbol{x}_1, \dots, \boldsymbol{x}_N$ with respect to a plane. This consists in finding $\overline{\boldsymbol{v}} \in \mathbb{S}^2$ a solution of the following minimization problem :

$$\min_{\boldsymbol{v} \in \mathbb{S}^2} \sum_{i=1}^{N} \operatorname{dist}\left(\boldsymbol{x}_i; \overline{\boldsymbol{x}} + (\boldsymbol{v}\mathbb{R})^\perp\right)^2,$$

where $(\boldsymbol{v}\mathbb{R})^\perp$ denotes the plane orthogonal to the vector $\boldsymbol{v}$. Similarly as before, we introduce the variance explained by the regression:

$$\sigma_{\Pi}^2 = \frac{1}{N-1} \sum_{i=1}^{N} |\boldsymbol{x}_i - \Pi \boldsymbol{x}_i|^2,$$

with Π being the orthogonal projection onto the optimal plane $\overline{\boldsymbol{x}} + (\overline{\boldsymbol{v}}\mathbb{R})^\perp$.

2. To check whether all NPs are on the same sphere, we proceed to a regression using a sphere as optimal set. For simplicity, we work directly on the distance of the positions to the mean position $\overline{\boldsymbol{x}}$.

$$\overline{\rho} = \frac{1}{N} \sum_{i=1}^{N} |\boldsymbol{x}_i - \overline{\boldsymbol{x}}|.$$

3. Similarly to the linear regressions, we introduce the explained variance for radial variations:

$$\sigma_\rho^2 = \frac{1}{N-1} \sum_{i=1}^{N} \left|\overline{\rho} - |\boldsymbol{x}_i - \overline{\boldsymbol{x}}|\right|^2$$

We compute the coefficient of determination associated to σ_{Π}^2 and σ_ρ^2, which determines whether the structure is close to a circle.

4. There remains to check if the magnetic moments are tangent to this circle. For this purpose, we compute the following scalar products (assuming $|\boldsymbol{m}| = 1$) :

$$S_r = \frac{1}{N} \sum_{i=1}^{N} \frac{\boldsymbol{x}_i - \overline{\boldsymbol{x}}}{|\boldsymbol{x}_i - \overline{\boldsymbol{x}}| + \varepsilon} \cdot \boldsymbol{m}_i.$$

Note that the regularization ε is mandatory to deal (numerically) with the particular case $\boldsymbol{x}_i = \overline{\boldsymbol{x}}$.

5. We introduce the ring estimator:

$$\mathfrak{R} = \left(1 - \frac{\sigma_{\Pi}^2}{\sigma^2}\right)\left(1 - \frac{\sigma_\rho^2}{\sigma^2}\right)\left(1 - S_r^2\right).$$

This metric achieves its maximal value when particle positions lie uniformly on a planar circle and the magnetic moments are tangent to this circle.

B.3. Identification of connected components

Although robust and effective for moderate system sizes, the estimators $\mathfrak{S}$ and $\mathfrak{R}$ exhibit limitations when applied to large-scale configurations, particularly for $N > 10$. In those cases, the emergence of disconnected structural components limits their diagnostic accuracy. Consequently, before evaluating $\mathfrak{S}$ and $\mathfrak{R}$, it is necessary to identify the connected components within the final configuration by analyzing inter-particle distances.

The threshold distance separating particles in physical contact – where the repulsive radial interaction balances the magnetic attraction – is determined numerically using simulations with $N = 2$, for which the connected spear configuration consistently emerges as the sole stable outcome. Independent *a posteriori* computations using theoretical estimates from [37] yielded comparable results. That work provides an explicit expression for the asymptotic inter-particle spacing in non-branching filaments as $N \to \infty$, involving Apéry's constant and depending on the physical parameters entering the model. They also establish convergence rates for straight and slightly curved filaments and show that the nearest-neighbor distance decreases monotonically with N. These mathematical results were used extensively during code development, in particular for validating the numerical computation of the threshold distance. The key estimate relevant here is that, when the repulsion parameter α in Eq. (5) satisfies $\alpha > 12$, the relative difference between the nearest-neighbor distances for $N = 2$ and $N = \infty$ remains below 2 %.

Based on this benchmark, we define the notion of *neighboring particles*. Specifically, two particles are classified as neighbors if the Euclidean distance between their centers is less than the reference contact distance determined for $N = 2$, augmented by a tolerance margin. Empirical testing guided the selection of a +70 % margin as a suitable threshold: larger margins (e.g., +100 %) tend to overestimate connectivity by including particles that are merely second-order neighbors, whereas smaller margins (e.g., below 50 %) generically underestimates connectivity by excluding particles at junction points.

A tolerance margin of +70 % for the threshold distance is not unique; a broad range of margins leads to essentially identical connectivity outcomes. To quantify this, we evaluate 500 steady-state configurations obtained as long-time limits of the evolution and compute the resulting connectivity for each chosen margin. To take into account the different possible cases, the number of NPs in these simulations ranges from $N = 2$ to $N = 25$, with N linearly distributed between these two extrema. Table 2 reports the deviations from the reference case +70 %. A false negative link refers to a pair of neighboring NPs identified as connected in the reference case but not under the tested margin. Conversely, a false positive link denotes a pair flagged as connected under the tested margin but not in the reference case. The results indicate a stable regime around the +70 % tolerance margin, suggesting that this choice reliably preserves the underlying neighbor structure. This quantitative analysis is complemented by direct inspection, confirming that the indicator aligns with the physical notion of a neighbor.

Once neighborhood relationships are established, the connected components of a given equilibrium structure are identified using a graph-theoretic approach. Particles are assigned to the same component if there exists a path of neighboring particles connecting them. Each component is then independently analyzed using the structural estimators $\mathfrak{S}$ and $\mathfrak{R}$.

Data availability

Data will be made available on request.

Table 2
Statistics of false neighboring links (relatively to the reference threshold of 70 %) for different values of the connectivity threshold. For each simulation, we compute the number of false positive and false negative links, relative to the number of particle pairs in a given simulation. Their averages over 500 simulations are reported in the table, in percentage relative to the reference.

Threshold	False negatives	False positives
50 %	7.51 %	
55 %	1.54 %	
60 %	0.25 %	
65 %	0.02 %	
70 %	**Reference**	**Reference**
75 %		0.01 %
80 %		0.06 %
85 %		0.23 %
90 %		0.44 %
95 %		13.14 %
100 %		88.06 %

References

[1] F.M. Koehler, M. Rossier, M. Waelle, E.K. Athanassiou, L.K. Limbach, R.N. Grass, D. Gunther, W.J. Stark, Chem. Commun. 32 (2009) 462.
[2] I. Rabias, D. Tsitrouli, E. Karakosta, T. Kehagias, G. Diamantopoulos, M. Fardis, D. Stamopoulos, T.G. Maris, P. Falaras, N. Zouridakis, N. Diamantis, G. Panayotou, D.A. Verganelakis, G.I. Drossopoulou, E.C. Tsilibari, G. Papavassiliou, Biomicrofluidics 4 (2010) 2411.
[3] K.E. Scarberry, E.B. Dickerson, J.F. McDonald, Z.J. Zhang, J. Am. Chem. Soc. 130 (2008) 10258.
[4] N. Parera Pera, Org. Biomol. Chem. 8 (2010) 2425.
[5] A. Ali, T. Shah, R. Ullah, P. Zhou, M. Guo, M. Ovais, Z. Tan, Y. Rui, Front. Chem. 9 (2021) 629054.
[6] S.M. Manishkumar, D. Yadav, Langmuir 40 (2024) 17239.
[7] R.P. Cowburn, M.E. Welland, Science 287 (2000) 1466.
[8] H. Zeng, J. Li, J.P. Liu, Z.L. Wang, S.H. Sun, Nature 420 (2002) 395.
[9] Y.R. Chemla, H.L. Grossman, Y. Poon, R. McDermott, R. Stevens, M.D. Alper, J. Clarke, Proc. Natl. Acad. Sci. USA 97 (2000) 14268.
[10] S. Bedanta, T. Eimuller, W. Kleemann, J. Rhensius, F. Stromberg, E. Amaladass, S. Cardoso, P.P. Freitas, Phys. Rev. Lett. 98 (2007) 176601.
[11] S. Wang, D. Wu F.J. Yue1, F.M. Zhang, W. Zhong, Y.W. Du, Appl. Phys. Lett. 94 (2009) 012507.
[12] H. Zeng, C.T. Black, R.L. Sandstrom, P.M. Rice, C.B. Murray, S. Sun, Phys. Rev. B 73 (2006) 020402.
[13] R.P. Tan, J. Carrey, C. Desvaux, J. Grisolia, P. Renaud, B. Chaudret, M. Respaud, Phys. Rev. Lett. 99 (2007) 176805.
[14] F. Hu, K.W. MacRenaris, E.A. Waters, E.A. Schultz-Sikma, A.L. Eckermann, T.J. Meade, Chem. Commun. 46 (2010) 73.
[15] C. Blanco-Andujar, D. Ortega, P. Southern, Q.A. Pankhurst, N.T.K. Thanh, Nanoscale 7 (2015) 1768.
[16] N.A. Usov, B. Ya. Liubimov, J. Appl. Phys. 112 (2012) 023901.
[17] Stefan Odenbach (Ed.), Ferrofluids: Magnetically Controllable Fluids and Their Applications, Vol. 594, Springer, 2008.
[18] John Philip, Magnetic nanofluids (Ferrofluids): Recent advances, applications, challenges, and future directions, Adv. Colloid Interface Sci. 311 (2023) 102810.
[19] J.F. Douglas, Nature 463 (2010) 302.
[20] J.E. Martin, Phys. Rev. E 79 (2006) 011503.
[21] A. Snezhko, I.S. Aranson, W.-K. Kwok, Phys. Rev. Lett. 96 (2006) 078701.
[22] A. Snezhko, I.S. Aranson, W.-K. Kwok, Phys. Rev. E 73 (2006) 041306.
[23] A. Snezhko, M. Belkin, I.S. Aranson, W.-K. Kwok, Phys. Rev. Lett. 102 (2009) 118103.
[24] M. Miller, D. Wales, J. Phys. Chem. B 109 (2006) 23109.
[25] J.D. Farrell, C. Lines, J.J. Shepherd, D. Chakrabarti, M.A. Miller, D.J. Wales, Soft Matter 9 (2013) 5407.
[26] D. Morphew, D. Chakrabarti, Soft Matter 12 (2016) 9633.
[27] S. Novikau, P.A. Sanchez, S.S. Kantorovich, J. Mol. Liq. 307 (2020) 112902.
[28] D. Rozhkov, E. Pyanzina, E. Novak, J. Cerda, T. Sintes, M. Ronti, P. Sanchez, S. Kantorovich, Mol. Simul. 44 (2018) 507.
[29] I. Novikau, E. Minina, P. Sanchez, S. Kantorovich, J. Magn. Magn. Mater. 498 (2020) 166152.
[30] Y. Xuan, M. Ye, Q. Li and, Int. J. Heat Mass Transfer 48 (2005) 2443.
[31] Y. Lalatonne, J. Richardi, M.P. Pileni, Nat. Mater. 3 (2004) 121.
[32] X. Xue, J. Wang, E.P. Furlani, ACS Appl. Mater. Interfaces 7 (2015) 22515.
[33] F.L. Durhuus, L.H. Wandall, M.H. Boisen, M. Kure, M. Beleggia, C. Frandsen, Nanoscale 13 (2021) 1970.
[34] Sofia S. Kantorovich, Alexey O. Ivanov, Lorenzo Rovigatti, Jose M. Tavares, Francesco Sciortino, Phys. Chem. Chem. Phys. 17 (25) (2015) 16601–16608.
[35] A.Y. Solovyova, E.A. Elfimova, Formation of magnetic nanoparticle aggregates and their magnetic response in a limited volume, Eur. Phys. J. Spec. Top. (2026) http://dx.doi.org/10.1140/epjs/s11734-026-02207-z.
[36] G. Klughertz, Ph.D. thesis, University of Strasbourg (2016).
[37] R. Côte, C. Courtes, G. Ferrière, L. Godard-Cadillac, Y. Privat, The Spear and the Ring, 2025, arXiv preprint arXiv:2504.02379.
[38] C. Iacovita, J. Hurst, G. Manfredi, P.-A. Hervieux, B. Donnio, J.-L. Gallani, M. Rastei, Nanoscale 12 (2020) 1842.
[39] G. Klughertz, P.-A. Hervieux, G. Manfredi, J. Phys. D: Appl. Phys. 47 (2014) 345004.
[40] F. Allouges, K. Beauchard, ESAIM: Cont. Opt. Cal. Var. 15 (2009) 676.
[41] G. Klughertz, G. Manfredi, P.-A. Hervieux, B.P. Pichon, S. Begin-Colin, J. Phys. Chem. C 120 (2016) 7381–7387.
[42] Walid Baaziz, Benoit P. Pichon, Solenne Fleutot, Yu Liu, Christophe Lefevre, Jean-Marc Greneche, Mohamed Toumi, Tahar Mhiri, Sylvie Begin-Colin, J. Phys. Chem. C 118 (2014) 3795–3810.
[43] Walid Baaziz, Benoit P. Pichon, Yu Liu, Jean-Marc Greneche, Corinne Ulhaq-Bouillet, Erwan Terrier, Nicolas Bergeard, Christine Boeglin Valerie Halté, Fadi Choueikani, Mohamed Toumi, Tahar Mhiri, Sylvie Begin-Colin, Chem. Mater. 26 (2014) 5063–5073.
[44] S. Sun, H. Zeng, J. Am. Chem. Soc. 124 (2002) 8204–8205.
[45] J. Park, et al., Nat. Mater. 3 (2004) 891–895.
[46] S. Laurent, et al., Chem. Rev. 108 (2008) 2064–2110.
[47] P. Guardia, et al., J. Mater. Chem. 22 (2012) 19971–19979.
[48] https://www.chemeo.com/cid/37-905-6/1-Octadecene#ref-kdb-pure.
[49] Geoffrey Cotin, Francis Perton, Corinne Petit, Sécou Sall, Céline Kiefer, Valentin Begin, Benoit Pichon, Christophe Lefevre, Damien Mertz, Jean-Marc Greneche, Sylvie Begin-Colin, Chem. Mater. 32 (2020) 9245–9259.
[50] Barbara Freis, Céline Kiefer, Maria de los Angeles Ramirez, Sébastien Harlepp, Damien Mertz, Benoit Pichon, Cristian Iacovita, Sophie Laurent, Sylvie Begin, Nanoscale 16 (2024) 20542–20555.
[51] https://www.chemeo.com/cid/19-460-0/Squalane.
[52] K. Butter, P.H.H. Bomans, P.M. Frederik, G.J. Vroege, A.P. Philipse, Nat. Mater. 2 (2003) 88.
[53] M.P. Arciniegas, A. Castelli, R. Brescia, D. Serantes, S. Ruta, O. Hovorka, A. Satoh, R. Chantrell, T. Pellegrino, Small 16 (2020) 1907419.
[54] D.H.E. Gross, Rep. Progr. Phys. 53 (1990) 605.
[55] D.H.E. Gross, P.-A. Hervieux, Z. Phys. D: Atoms, Mol. Clust. 35 (1995) 27.
[56] T. Sauer, Handbook of Comp. Fin., 2012, pp. 529–550.
[57] D.J. Higham, SIAM Rev. 43 (3) (2001) 525.